

Sensitivity of snowfall forecast over North China to ice crystal deposition/sublimation parameterizations in the WSM6 cloud microphysics scheme

Zhanshan Ma^{1,2,3,4} | Jason A. Milbrandt⁴ | Qijun Liu^{2,3} | Chuanfeng Zhao¹ |
 Zhe Li^{2,3} | Fa Tao⁵ | Jian Sun^{2,3} | Xueshun Shen^{2,3} | Qi Kong² | Feifei Zhou^{2,3} |
 Liping Huang^{2,3} | Kan Dai² | Leqiang Sun⁴ | Jiong Chen^{2,3} | Qingu Jiang^{2,3} |
 Hao Fan¹ | Yikun Yang¹ | Xiangfeng Hu⁶

¹State Key Laboratory of Earth Surface Processes and Resource Ecology, and College of Global Change and Earth System Science, and Joint Center for Global Change Studies, Beijing Normal University, Beijing, China

²National Meteorological Center, Beijing, China

³Numerical Weather Prediction Center of China Meteorological Administration, Beijing, China

⁴Meteorological Research Division, Environment and Climate Change Canada, Dorval, Quebec Canada

⁵Meteorological Observation Center of China Meteorological Administration, Beijing, China

⁶Hebei Meteorological Service, Hebei, China

Correspondence

C. Zhao, State Key Laboratory of Earth Surface Processes and Resource Ecology, and College of Global Change and Earth System Science, and Joint Center for Global Change Studies, Beijing Normal University, Beijing 100875, China.

Email: czhao@bnu.edu.cn

Funding information

Ministry of Science and Technology of the People's Republic of China, Grant/Award Numbers: 2017YFC1501406, 2017YFC1502001, 2018YFC1505702, 2019YFA0606803; National Natural Science Foundation of China, Grant/Award Numbers: 41925022, 42075155, 42090032

Abstract

Ice-phase cloud microphysical processes are very complicated, and there are still many uncertainties in current microphysics parameterization schemes. In this study, two alternative ice crystal deposition/sublimation (ICDS) parameterizations, following the Harrington *et al.*, *Journal of the Atmospheric Sciences*, 1995, 52, 4344–4366 and Koenig, *Monthly Weather Review*, 1972, 100, 417–423 methods, were implemented into the Weather Research and Forecast (WRF) Single-Moment 6-class Microphysics (WSM6) scheme in the Global/Regional Assimilation and Prediction System (GRAPES) regional operational model to investigate their impact on overestimation of snowfall over North China. The results show that the snowfall amount and cloud particle composition are very sensitive to the ICDS parameterization. Sensitivity tests with WSM6 using the Harrington and Koenig ICDSs, referred to as WSM6_H and WSM6_K, respectively, notably reduced overestimation of the snowfall amount and simulated more realistic supercooled cloud water content compared with ERA5 reanalysis data. The vertical distributions, intensities, and duration of radar echoes simulated by WSM6_H are the most consistent with millimeter-wavelength cloud radar observations. There is competition for water vapor in WSM6 due to the sequential order in which processes are updated. This tends to weaken the deposition of snow and graupel and the condensation of cloud water when the deposition of ice crystals is too strong in a cold region. In both WSM6_H and WSM6_K, the deposition processes of ice crystals are reduced and the other microphysical transformation processes become more active compared with WSM6. Overall, the WSM6_H configuration improves the forecast performance as evaluated by Taylor diagrams for eight snowfall days over North China. The ICDS parameterizations must therefore be handled carefully due to their large uncertainties in the development of the cloud microphysics schemes.

KEY WORDS

GRAPES, ice crystal deposition/sublimation parameterization, snowfall, water vapor competition, WSM6 cloud microphysics scheme

1 | INTRODUCTION

As a main weather forecasting tool, the performance of numerical weather prediction (NWP) models directly affects the accuracy of forecasts (Linus and Erland, 2013; Bauer *et al.*, 2015). Quantitative precipitation forecasting (QPF) remains one of the greatest challenges among all the forecasting elements. The use of different models or different cloud microphysics parameterization schemes in the same model is apt to produce significantly different QPFs (Morrison *et al.*, 2009; Milbrandt *et al.*, 2010; Molthan and Colle, 2012; Cintineo *et al.*, 2014; Fernández-González *et al.*, 2015).

With the rapid progress of high-performance computers, the horizontal grid spacing of mesoscale NWP models has been continuously improved to kilometer or sub-kilometer scales, approaching the cloud-resolving scale. As such, most high-resolution NWP models do not use convective parameterization schemes; rather, clouds and precipitation are represented only by cloud microphysics schemes. Therefore, more realistic microphysics schemes are beneficial to QPF (e.g., Barszcz *et al.*, 2018; Yu *et al.*, 2019). Precipitation in a microphysics scheme comes from the sedimentation of different types of hydrometeor categories, each of which undergoes microphysical processes, such as condensation/evaporation, deposition/sublimation, autoconversion, collision-coalescence, freezing and melting, etc. (Hong *et al.*, 2004; Thompson *et al.*, 2004; Morrison and Milbrandt, 2015). For most current bulk schemes, the treatments of liquid-phase microphysical processes are not very different since their physics is relatively well understood. Because ice-phase particles have very complicated habits (shapes, mass, densities and fall speeds, etc.) and their growth and conversion processes are affected by their microscopic characteristics and the environmental conditions, the use of different microphysics schemes results in significant differences in the treatment of ice-phase processes, which ultimately impacts QPF (Iguchi *et al.*, 2012; Kang *et al.*, 2018).

Snowfall is one of the most important weather phenomena in winter. However, less attention has been paid to the verification and diagnosis of snowfall forecasts as well as the optimization of the corresponding physical processes because snowfall is not as frequent or violent as heavy summer precipitation. Moreover, due to the large density difference between snow and liquid water (Roebber *et al.*, 2003), relatively small biases in the QPF could produce large differences in actual snowfall depth. Therefore, verification of the impact of ice-phase cloud microphysical processes on snowfall forecast and the corresponding optimization should improve QPF.

Recent research has focused on the evaluation, diagnosis, and optimization of the influence of

ice-phase microphysical processes on the snow forecast performance of NWP models. Several studies have evaluated the impacts of different cloud microphysics schemes on snowfall amount and hydrometeor content (Fernández-González *et al.*, 2015; McMillen and Steenburgh, 2015; Comin *et al.*, 2018; Merion *et al.*, 2019). For example, McMillen and Steenburgh (2015) investigated the impact of microphysics parameterizations on simulations of the Great Salt Lake-effect snowstorms and found that the precipitation simulated using four microphysics schemes varied in terms of coverage, amount, and position. The Thompson scheme yielded the best estimates versus radar-derived precipitation and gauge observations, while the Weather Research and Forecasting (WRF) Double-Moment 6-class (WDM6) schemes produced the largest overprediction. Molthan *et al.* (2016) examined whether selected cloud microphysics schemes can reproduce key characteristics of the observed reflectivity distributions and fall speed within various categories of observed riming. There are also studies that have improved the performance of snowfall forecast by optimizing the ice-phase parameterizations of snow density, ice nucleation, autoconversion, size distribution parameters of snow and rain, and melting and refreezing of ice particles (Roebber *et al.*, 2003; Thompson *et al.*, 2004; Thériault and Stewart, 2010). In China, most studies have considered the differences in snowfall amount and hydrometeor content when simulated using various schemes (Sun *et al.*, 2007; Li *et al.*, 2011; Wu *et al.*, 2011; Yu *et al.*, 2017). For example, Wang *et al.* (2014) found that the WRF Single-Moment 3-class (WSM3) scheme overestimated the ice concentration of a snowstorm in the Qinghai-Xizang Plateau, while the precipitation could be improved by adjusting the relationship between the ice concentration and surface saturation.

The Numerical Weather Prediction Center (NWPC) of the China Meteorological Administration (CMA) has been devoted to developing its own NWP system since the 2000s. At present, a complete numerical forecasting system has been established including global medium-range, regional, and ensemble simulations based on the Global/Regional Assimilation and Prediction System (GRAPES), with steadily improved prediction performance (Chen *et al.*, 2016a; Shen *et al.*, 2007; Huang *et al.*, 2017; Ma *et al.*, 2018; Zhang *et al.*, 2019; Chen *et al.*, 2020; Ma *et al.*, 2021a, 2021b). Among these, the GRAPES Regional High Resolution Deterministic Prediction System (GRHRDPS) became operational in June 2018, acting as a source of numerical guidance for forecasters. The GRAPES 3 km model uses the WRF Single-Moment 6-class (WSM6, Hong *et al.*, 2004) scheme. Although this scheme shows good performance for equitable threat scores (ETS) of precipitation in warm seasons, it has

significantly overestimated the precipitation in northern China repeatedly in cold seasons. There is an urgent need to solve this problem to improve the snowfall forecast performance as well as the meteorological support capability for outdoor winter activities, including the upcoming Beijing 2022 Winter Olympics. Previous studies have also found that supercooled liquid water contents simulated by WSM6 are significantly underestimated compared with other schemes (figure 4 in Fernández-González *et al.*, 2015; figure 3 in Molthan *et al.*, 2016; figure 4 in Nie *et al.*, 2016; table 4 in Morrison *et al.*, 2015), which is most likely related to the ice-phase processes. It has been shown that the growth of ice due to cloud deposition in WSM6 is significantly larger than that in other schemes (Ma *et al.*, 2021a).

In this article, we implemented two different ice crystal deposition/sublimation (ICDS) parameterizations in the WSM6 scheme to conduct sensitivity tests to investigate their effects on the prediction of snowfall amount and hydrometeor water content in GRHRDPS. The remainder of this article is organized as follows: GRHRDPS and the adopted ICDS parameterizations are described in the next section. Section 3 describes the experimental configurations, analysis methods, and datasets. The experimental results of ICDS, as well as their impacts on macroscopic and microphysical cloud and snowfall fields, are presented in Section 4. A discussion and concluding remarks are provided in the final section.

2 | MODEL DESCRIPTION AND ICDS PARAMETERIZATIONS

2.1 | GRHRDPS

GRHRDPS is a regional NWP system that includes both an atmospheric model and a data assimilation component. The framework of the atmospheric model is a fully compressible, nonhydrostatic dynamical core utilizing potential temperature, specific humidity, three-dimensional wind field components, and dimensionless air pressure (Exner function) as independent prognostic variables. Based on a latitude-longitude grid, the model discretizes the spatial variables on a staggered Arakawa-C grid and employs an off-center two-time-level semi-implicit time discretization with semi-Lagrangian advection. In the vertical direction, the height-based terrain-following coordinate with Charney-Phillips variable staggering is adopted in this model. The piecewise rational method (PRM) scalar (Su *et al.*, 2013) has been introduced to compute the advection of the moisture field.

The physical parameterization schemes used in the operational GRHRDPS include the RRTM long-wave

radiation scheme (Mlawer *et al.*, 1997), Dudhia short-wave radiation scheme (Dudhia, 1993), NOAH land surface scheme with four-layer soil temperature and moisture model (Chen and Dudhia, 2001), MRF planetary boundary layer scheme (Hong and Pan, 1996), and WSM6 micro-physics scheme (Hong *et al.*, 2004). GRHRDPS covers the entire China domain with a horizontal grid spacing of 0.03° and 50 vertical levels. The convective convection parameterization is not used.

2.2 | ICDS parameterizations

2.2.1 | The original ICDS parameterization

As described by Hong *et al.* (2004), the original ice crystal deposition/sublimation rate by deposition of water vapor (\dot{r}) in the WSM6 scheme is determined by a method of diffusion balance following Mason (1971) and Dudhia (1989). When the air is supersaturated with respect to ice, this is obtained by using the mean mass of an ice crystal M_I and the mass-diameter relationship,

$$\dot{r} = \frac{4\bar{D}_I(S_I - 1)N_I}{A_I + B_I} = \frac{4\bar{D}_{I_{con}}(S_I - 1)(\rho_a q_I N_I)^{0.5}}{A_I + B_I} \quad (1)$$

where S_I is the ice saturation, ρ_a is air density, q_I is the mixing ratio of ice crystal, and A_I and B_I are thermodynamic functions.

$$A_I = \frac{L_s^2 \rho_a}{K_a R_v T^2} \quad (2)$$

$$B_I = \frac{1}{P_{si} D_v} \quad (3)$$

where K_a is the thermal conductivity of air and D_v is the diffusivity of water vapor in air. L_s is the latent heat of sublimation, R_v is the gas constant for water vapor, P_{si} is the saturation vapor pressure over ice, T is the air temperature. N_I is the ice crystal number concentration, which is diagnosed from the ice mass by

$$N_I = 5.38 \times 10^7 (\rho_a q_I)^{0.75} \quad (4)$$

\bar{D}_I is the mean diameter of an ice crystal, which can be obtained for a hexagonal plate by using a diameter-mass relationship (Rutledge and Hobbs, 1983)

$$\bar{D}_I = \bar{D}_{I_{con}} M_I^{1/2} \quad (5)$$

$\bar{D}_{I_{con}}$ is set as 11.9 in the WSM6 scheme instead of the value of 16.3 used in Rutledge and Hobbs (1983) and Dudhia (1989). The relationship between the mean mass (M_I)

and N_I is

$$M_I = \left(\frac{\rho_a q_I}{N_I} \right) \quad (6)$$

Substituting Equations (5) and (6) into Equation (1) yields

$$\dot{r} = \frac{4\bar{D}_{I_{con}}(S_I - 1)(\rho_a q_I N_I)^{0.5}}{A_I + B_I} \quad (7)$$

This formula also applies in subsaturated conditions where the ICDS rate is negative, representing sublimation.

2.2.2 | The Harrington ICDS parameterization

In the Harrington scheme (Harrington *et al.*, 1995), the mixing ratio tendency of ice crystal (\dot{r}) can be described by

$$\dot{r} = \frac{1}{\rho_a} \int_0^\infty \frac{dm}{dt} n(D) dD \quad (8)$$

where ρ_a is the density of air, $\frac{dm}{dt}$ is the mass growth rate of ice crystal, and $n(D)$ is the size distribution.

The equation for the mass growth rate of ice particles which only considers vapor growth takes the form (Byers, 1965)

$$\frac{dm}{dt} = 4\pi C_i(S_I - 1) G_i(T, P) \bar{f}_{v,L^*} \quad (9)$$

where C_i is the crystal capacitance term, \bar{f}_{v,L^*} is the ventilation coefficient, and $G_i(T, P)$ is a function of temperature and pressure, defined as (Pruppacher and Klett, 1978)

$$G_i(T, P) = \left[\frac{R_v T}{q_{si} D_v} + \frac{L_s}{K_a T} \left(\frac{L_s}{R_v T} - 1 \right) \right]^{-1} \quad (10)$$

where the meanings of the variables are the same as in Equations (2) and (3). The ventilation coefficient \bar{f}_{v,L^*} used here is for oblate spheroids and follows the formulation given by Pruppacher and Klett (1978). It adopts the method of Walko *et al.* (1995), which uses a bounded value to the reference temperature in the expansion of the Clausius–Clapeyron equation to obtain a more accurate form of the vapor depositional growth relationship. Moreover, because the capacitance term C_i in (9) is a function of a maximum and minimum dimension, c and a , respectively, it can be simplified by writing C_i as a function of the aspect ratio $A = c/a$ and its maximum dimension $c = D$ to obtain an analytical solution to (8)

$$C_i = C_i(c, a) = g(A, D) = \chi(A)D \quad (11)$$

where $\chi(A)$ is a function of the aspect ratio. The function is a constant function of a given aspect ratio, which allows

the dm/dt equation to be integrated over the distribution functions.

Substituting Equations (9) and (11) into Equation (8), we get

$$\dot{r} = \frac{\Psi}{\rho_a} \frac{N_I}{\Gamma(v)} D_n \Gamma(v+1) = \frac{\Psi}{\rho_a} I(1). \quad (12)$$

which is the expression used for the vapor depositional growth of a given size distribution, where

$$\Psi = 4\pi \chi(A)(S_I - 1) G_i(T, P) \bar{f}_{v,L^*}$$

N_I is the diagnosed value used in WSM6 as in Hong *et al.* (2004). D_n is related to the mean ice crystal size \bar{D} of the number distribution,

$$\bar{D} = \frac{\int_0^\infty D n(D) dD}{\int_0^\infty n(D) dD} = v D_n \quad (13)$$

where v is the distribution shape parameter. For ice crystal, we set v equal to 1 based on Hobbs (1974) and Hu and He (1988). Since the size distribution of ice crystals is not specified in the WSM6 scheme, the setting of v is only used when calculating the Harrington ICDS parameterization while we ignored its impact on the other microphysical processes related to ice crystals (e.g., fall speed and collection processes) in this study.

$\Gamma(v)$ is the complete gamma function, whose definition can be found from Abramovitz and Stegun (1972)

$$\Gamma(v) = \int_0^\infty D^{v-1} \exp(-D) dD \quad (14)$$

$I(P)$ in Equation (12) is given by the moments of the gamma distribution as

$$I(P) = \int_0^\infty D^P n(D) dD = \frac{N_t}{\Gamma(v)} D_n^P \Gamma(v+P) \quad (15)$$

2.2.3 | The Koenig ICDS parameterization

In the Koenig (1972) parameterization, the deposition rate of ice crystal is solely a function of temperature. The ice crystal growth rate in a water-saturated environment under different ambient temperatures follows an exponential dependence on mass, expressed as

$$\frac{dm_i}{dt} = a_1 \cdot m_i^{a_2} \quad (16)$$

where a_1 and a_2 are (temperature sensitive) diffusion growth parameters, whose values are given for different temperatures to approximate the growth behavior of a

crystal growing by diffusion. The deposition rate of an ice population in an environment with any specific humidity (q_v) and temperature can then be deduced (Hu and He, 1988) as

$$\dot{r} = \int_0^\infty N_0 D \exp(-\lambda D) a_1 (A_{mi} D^2)^{a_2} \frac{q_v - q_{si}}{q_{sw} - q_{si}} dD = A_{vi} (q_v - q_{si}) \quad (17)$$

where

$$A_{vi} = \frac{2a_1 N_I (6N_I/q_I)^{-a_2}}{(q_{sw} - q_{si})} \quad (18)$$

q_{sw} and q_{si} are the saturation vapor pressure over water and over ice, respectively.

3 | METHODOLOGY AND DATASETS

3.1 | Experimental configurations

The GRHRDPS v4.3 operational version is used in the present study with physical process settings consistent with those described in Section 2.1. Since the 3Dvar data assimilation system with cloud analysis scheme often diagnoses hydrometeors in the initial analysis field, it generally tends to increase the precipitation amount forecast at the early stage of integration (Zhu *et al.*, 2017). To simplify the sensitivity analysis on the overestimation of snowfall in the WSM6 scheme, all experiments are carried out only using the analysis and forecast fields of the National Centers for Environmental Prediction Global Forecast System (NCEP/GFS) as the initial conditions and time-varying lateral boundary conditions at 6-hr intervals, without 3Dvar data assimilation. All simulations are run at 0.03° horizontal grid spacing resolution with $1,001 \times 1,501$ grid points in the south–north and east–west directions, respectively. The vertical layers are set as 50 stretched sigma levels up to the model top at 10 hPa. The simulation domain covers the North China Plain and surrounding areas. The integration time step is 30 s. To analyze the sensitivity of the snowfall amount forecast to the ICSD parameterizations in detail, a snowfall case from November 29 to 30, 2019 is examined. The model starts at 0000 UTC 29 November and is integrated up to 24 hr with 1-hr interval outputs. In addition, simulations for all six snowfall cases with eight snowfall days that occurred in the study area from November 2019 to February 2020 are conducted under the same configurations to obtain a more robust result for the sensitivity experiment.

3.2 | Analysis methods

3.2.1 | Microphysical budget analysis

A microphysical budget analysis method as proposed by Colle and Zeng (2004a, 2004b) and Colle *et al.* (2005) is adopted in this study. This is an effective tool to help determine the relative importance of each microphysical process in transferring water mass from one category to another by quantifying the relationship between water species (Colle and Zeng, 2004a, 2004b; Colle *et al.*, 2005; Aligo, 2011; Jouan and Milbrandt, 2019). To determine their relative importance, each microphysical process MR_{xy} listed in the Appendix was normalized by the integrated water vapor loss (WVL) within the same box by

$$MR_{xy} = \frac{\sum_{i,j,k} QMR_{xy}(i,j,k) \rho_a(i,j,k) \Delta\sigma(k)}{\sum_{i,j,k} WVL(i,j,k) \rho_a(i,j,k) \Delta\sigma(k)} \times 100\% \quad (19)$$

where QMR_{xy} is the conversion rate of a specific microphysical process, ρ_a is the air density, $\Delta\sigma$ is the height difference of two sigma levels of the model, and WVL is the total water vapor loss rate, computed as the sum of all the sink terms in the water vapor budget. Since six sink terms of water vapor are considered in WSM6, including condensation of cloud water (ccond) and rain (rcond), ice nucleation (pvi), and deposition of ice (idep), snow (sdep), and graupel (gdep), WVL is calculated as

$$WVL = ccond + rcond + pvi + idep + sdep + gdep \quad (20)$$

Each normalized microphysical tendency ratio in the following analysis is the temporal and spatial mean.

3.2.2 | Snowfall verification method

The Taylor diagram is employed to evaluate the overall impacts on the snowfall of the different ICDS parameterizations. Taylor diagrams have been designed to provide a concise, graphical statistical summary of two (or more) fields (Taylor, 2001). They are especially useful for quantifying the correspondence between modeled and observed behavior in terms of three statistics: the Pearson correlation coefficient, the centered root-mean-square difference, and the standard deviation. They are widely adopted to assess the performance of atmospheric models (IPCC, 2001; Pincus *et al.*, 2008; Wu *et al.*, 2012; Fernández-González *et al.*, 2015; Zhao *et al.*, 2020).

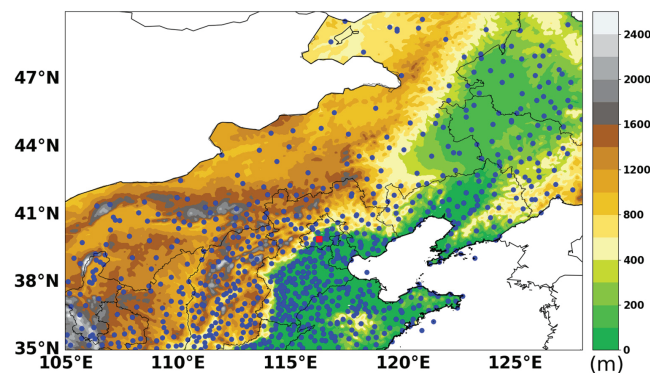


FIGURE 1 Topography height (unit: m) and observation stations in the simulation domain. Blue circles represent locations of precipitation gauges, while the red square denotes location of MMCR

3.3 | Verification datasets

3.3.1 | Gauge precipitation

With the aim of quantitative validation of the daily precipitation amount as simulated using the different ICDS parameterizations in the GRHRDPS, we used a daily accumulated precipitation database from the CMA precipitation gauge network, as applied by Su *et al.* (2020). The intelligent weighing precipitation measuring instruments are used. There are a total of 761 gauges in the study area, as shown in Figure 1.

3.3.2 | MMCR reflectivity

Millimeter-wavelength cloud radar (MMCR) is a widely used and reliable instrument for measuring the vertical structure and the macroscopic and microphysical properties of clouds since it can penetrate and detect the cloud interior with shorter wavelength compared with conventional weather radars (Zhao *et al.*, 2012; 2016; 2017; Chen *et al.*, 2016b). In the study area, the simulated radar reflectivity from the model is compared with those retrieved from a ground-based MMCR located at Beijing Southern Suburb Atmospheric Observation Base (BSSAOB), shown by a solid red square in Figure 1. The technical specifications of the MMCR are summarized in Table 1. The total equivalent radar reflectivity factor (in $\text{mm}^6 \text{ m}^{-3}$) of the model was calculated following Stoelinga (2005), which is the sum of the equivalent reflectivity from all hydrometeor species except for cloud water. The simulated reflectivity at the MMCR site location is further derived with a linear interpolation and compared with the MMCR observations.

3.3.3 | ERA5 reanalysis data

Because existing cloud observation methods seldom measure the macro- and microphysical variables of large-scale clouds simultaneously, it is difficult to verify accurately the cloud properties in NWP models. Under these circumstances, reanalysis data are often used to evaluate models. The European Centre for Medium-Range Weather Forecast (ECMWF) released its fifth-generation global climate reanalysis dataset called ERA5 in 2018 (Hersbach *et al.*, 2020), which has better analysis quality compared with its predecessors (Dee *et al.*, 2011), using cycle 41r2 of the Integrated Forecasting System (IFS) (Hersbach *et al.*, 2019). ERA5 benefits from improvements to the microphysics scheme in the IFS (Hersbach *et al.*, 2020), a more detailed representation of mixed-phase clouds (Forbes and Ahlgrimm, 2014), new prognostic variables for precipitating rain and snow (Forbes *et al.*, 2011; Forbes and Tompkins, 2011), and the parameterizations of warm-rain processes and ice-phase process (Ahlgrimm and Forbes, 2014). The ERA5 dataset can thus provide the vertical distributions of four types of hydrometeors, viz. cloud water, rain, ice, and snow, as well as their column-integrated contents. The horizontal grid spacing is $0.25^\circ \times 0.25^\circ$, with vertical coverage from 1,000 to 1 hPa and temporal resolution of 1 hr.

4 | RESULTS

4.1 | The synoptic pattern and its simulation performance

The synoptic pattern associated with this snowfall case is shown in Figure 2. The circulation over North China was characterized by a mid-level trough that came from Central Mongolia and the shear convergence of a low-level jet. The convergent upward motion ahead of the trough provided dynamic conditions and the southwest flow as the main source of water vapor. During the eastward movement of the trough, the entrained westward cold air converges with the warm and humid air brought by the low-level flow.

The ability to simulate the large-scale flow is necessary for detailed analysis of the microphysics. To investigate the model performance of the three simulations with respect to the large-scale conditions, we compared the wind, geopotential height, and relative humidity fields after 12 hrs of integration with those from the National Center for Environmental Prediction (NCEP) Final Operational Global Analysis (FNL) data, shown in Figure 3. The three runs simulated the large-scale conditions reasonably

TABLE 1 The main technical specifications of the MMCR at BSSAOB, Beijing, China

Order	Item	Technical specifications
1	Radar system	Coherent, pulsed Doppler, solid-state transmitter, pulse compression
2	Radar frequency	$35 \text{ GHz} \pm 200 \text{ MHz}$ (Ka band)
3	Detecting parameters	Z , V_r , S_w , L_{DR} , S_z
4	Detection capability	$<-30 \text{ dBZ}$ at 5 km
5	Location information	(116.47° E , 39.81° N), altitude 32 m
6	Range of detection	Height: 0.120–15 km Reflectivity: -50 dBZ to $+30 \text{ dBZ}$ Height resolution: 30 m Temporal resolution: 60 s (adjustable) Transmit power stability: 0.22% (dBm) Calibration precision of reflectivity factor: 0.15 dBZ

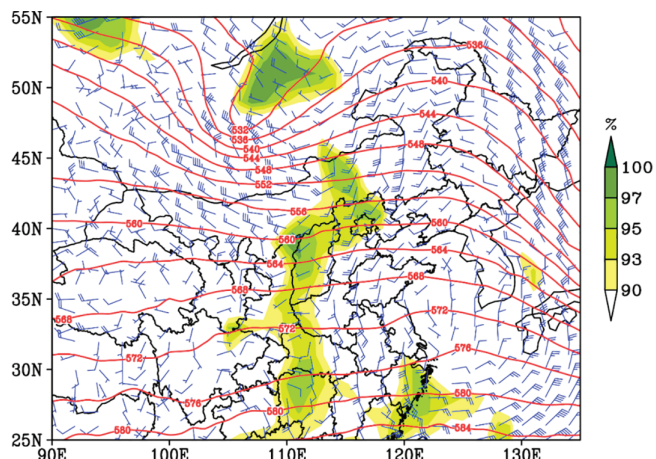


FIGURE 2 Synoptic features of wind (blue barbs), relative humidity (shaded, %) at 850 hPa, and geopotential height (red solid contours, 10 gpm) at 1200 UTC on November 29, 2019

well, with sufficient overall quality to allow us to proceed with the microphysical analysis. The differences in the relative humidity field between the three runs are related to the deposition/sublimation rates of ice crystal, as explained below in the section on the microphysical budget.

4.2 | Snowfall quantity

Figure 4 shows the observed and simulated 24-hr accumulated snowfall amount from 0000 UTC November 29 to 0000 UTC November 30, 2019. According to the meteorological observation standard of the CMA, snowfall events with 24-hr accumulated liquid-equivalent precipitation of 0.1–2.5 mm, 2.5–5 mm, 5–10 mm, and over 10 mm are

defined as light snow, moderate snow, heavy snow, and torrential snow, respectively. As shown in Figure 4a, snowfall during this episode occurred mainly in $105^\circ\text{--}125^\circ \text{ E}$ and $35^\circ\text{--}50^\circ \text{ N}$, with the main level being light snow. The high-value areas are mainly concentrated in $108^\circ\text{--}120^\circ \text{ E}$ and $38^\circ\text{--}43^\circ \text{ N}$, with moderate and heavy snow locally.

The 24-hr snowfall coverage in the WSM6_ORG experiment is in good agreement with the observations, but the amount is significantly overestimated. In most areas, the simulated amount lies within 2.5–10 mm, which is moderate or heavy snow. In the areas with large values of observational precipitation (5–10 mm), the simulated snowfall amount is mostly greater than 10 mm, and even above 20 mm in some places. The 24-hr domain-averaged amount ($105^\circ\text{--}125^\circ \text{ E}$, $35^\circ\text{--}47^\circ \text{ N}$) is 2.54 mm, which is much higher than the observed value (1.46 mm). Also, the maximum simulated snowfall amount (27.8 mm) is much larger than the observed maximum of 11.7 mm. For the simulations using the Harrington and Koenig ICDS parameterizations in the WSM6 scheme (WSM6_H and WSM6_K), the overestimation from the original scheme is significantly reduced (Figure 4c,d). The snowfall amount simulated by both modified configurations shows decreases, but with some differences. The WSM6_H simulated snowfall area is in good agreement with the observation. Both the regional averaged amount (1.55 mm) and the maximum amount (13.43 mm) are closer to the observations than those of the WSM6_ORG. The WSM6_H-simulated snowfall area with amounts above 5 mm corresponds well with the observations, but the range is slightly larger. In the area of $43^\circ\text{--}47^\circ \text{ N}$ and $118^\circ\text{--}123^\circ \text{ E}$, the snowfall amount is still overestimated by WSM6_H. In this area, the observations show that moderate snow only appears locally. However, WSM6_H

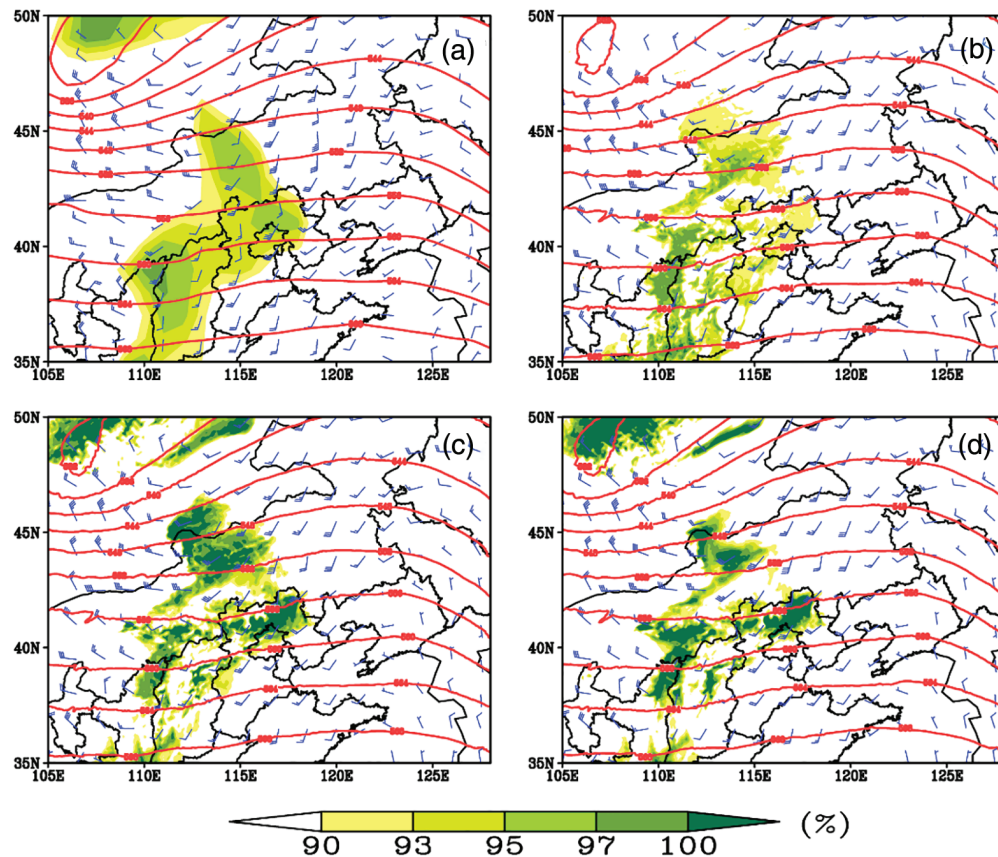


FIGURE 3 Same as Figure 2, but for the (a) FNL data, and three experiments (b) WSM6_ORG, (c) WSM6_H, and (d) WSM6_K

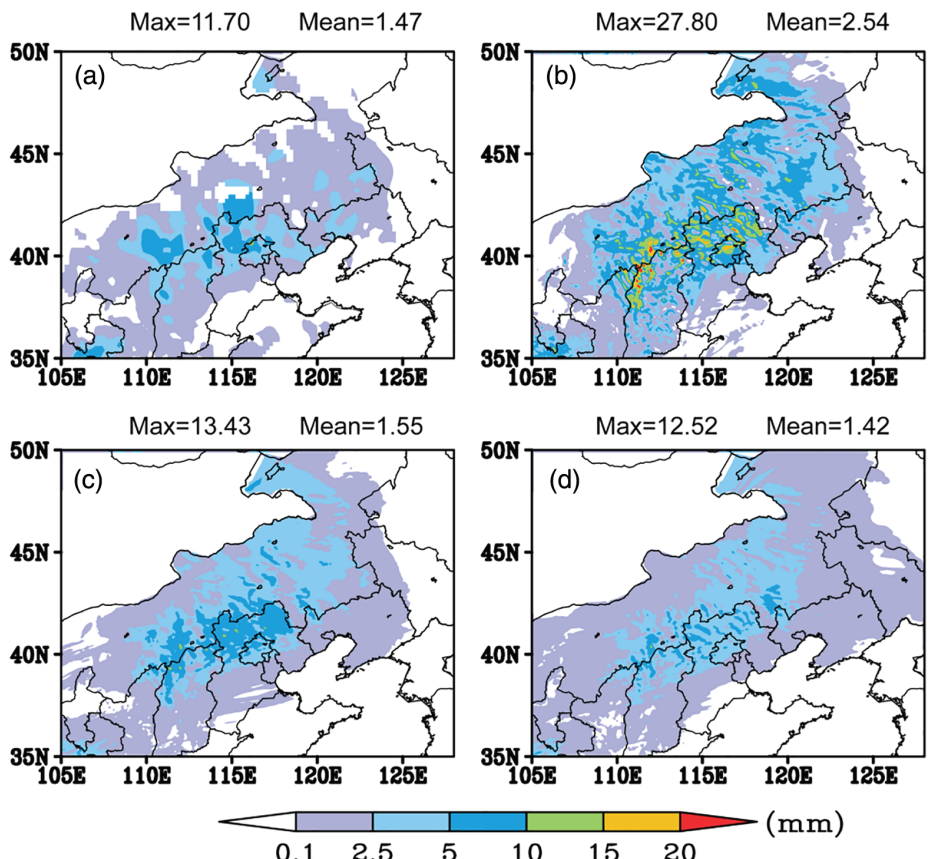
simulates a larger area of moderate snow. This area is grassland in Inner Mongolia with sparse population and relatively few observation stations (Figure 1), so there are large uncertainties in the observations. The WSM6_K-simulated snowfall amount is the lowest among the three experiments, with the regional averaged snowfall (1.42 mm) and maximum snowfall (12.52 mm) both closest to the observations. The areas of moderate and heavy snow simulated by WSM6_K fit the observations the best, but the range of heavy snow is narrower than in the observations. Similar to the WSM6_H simulation, the WSM6_K-simulated snowfall area in Inner Mongolia is also slightly larger than the observations. Note that there are some false forecasts of light snow east of 124° E.

Overall, both the WSM6_H and WSM6_K configurations succeed in reducing the overestimation of snowfall in the WSM6_ORG simulation. Regarding the snowfall distribution and magnitude, WSM6_H performs the best among the three experiments. Its snowfall coverage and amount correspond well with the observations. In contrast, the WSM6_K scheme overestimates the snowfall coverage and underestimates the snowfall amount in the large-value center.

In cloud microphysical schemes, the simulated precipitation comes from the total mass flux at the lowest

model level (near the surface) from all sedimenting hydrometeor categories. To analyze the impacts of the Harrington *et al.* (1995) and Koenig (1972) ICDS parameterizations on the surface precipitation, the accumulated precipitation from four types of hydrometeor (rain, ice, snow, and graupel) are outputted separately. Figure 5 shows the temporal evolution of the domain-averaged total precipitation and precipitation in the four categories in the snowfall area of 35°–50° N, 105°–125° E. It can be seen that the total precipitation from WSM6_ORG is 2.18 mm, coming mainly from ice and snow. The 24-hr averaged precipitation amounts of snow and ice are 1.5 and 0.65 mm, respectively. The contribution of graupel is negligible. In the WSM6_H and WSM6_K experiments, the total and individual precipitation are both different from WSM6_ORG. The graupel precipitation in WSM6_H and WSM6_K increases significantly, while their snow and ice precipitation amounts decrease correspondingly. In WSM6_H, the graupel precipitation is 0.2 mm, while the snow precipitation is reduced to 0.8 mm. The ice precipitation increases slightly to 0.75 mm. The 24-hr averaged total precipitation in the WSM6_H simulation is 1.75 mm, a notable decrease compared with WSM6_ORG. In WSM6_K, the graupel precipitation is 0.45 mm and the corresponding precipitations

FIGURE 4 Observed (a) and simulated (b–d) 24-hr accumulative precipitation (unit: mm) from 0000 UTC 29 November to 0000 UTC on November 30, 2019: (a) observation, (b) WSM6_ORG, (c) WSM6_H, and (d) WSM6_K



of snow and ice decrease to 0.79 and 0.41 mm, respectively. Its 24-hr total precipitation is 1.65 mm. The reason for these changes is that the transformation processes to graupel are significantly increased when using the Harrington and Koenig ICDS parameterizations in WSM6. This is illustrated further in the analysis of the microphysical budget in Section 4.4.

4.3 | Hydrometeor mass distribution

In this section, the sensitivities of the total column mass content and vertical distribution of the hydrometeors to the ICDS parameterization used in the WSM6 scheme are analyzed. The impact of the ICDS parameterizations on the underestimation of supercooled liquid water simulated by the original WSM6 scheme in previous studies (Fernández-González *et al.*, 2015; Morrison *et al.*, 2015; Molthan *et al.*, 2016; Nie *et al.*, 2016) is also investigated. Figure 6 shows the horizontal distributions of the 24-hr average column liquid water content (CLWC) and column solid water content (CSWC) in the ERA5 data and the three simulations. The CLWCs of the ERA5 data and the WSM6 scheme are both composed of the column content of cloud water and rain. The CSWC in WSM6 is the sum of the column content of ice, snow, and graupel. Since the solid

hydrometeors in the ERA5 data include only ice crystal and snow, the ERA5 CSWC is the total of these two column contents. The column contents, CC_x , of each hydrometeor category x were calculated as

$$CC_x = \sum_{k=1}^{k=n_{top}} \rho_a \cdot q_x \cdot \Delta\sigma(k) \quad (21)$$

where q_x is the mass mixing ratio, ρ_a is the air density, $\Delta\sigma$ is the height difference between two sigma levels, and n_{top} is the total number of model levels.

It can be seen that the CLWC in the ERA5 data is larger in the south and smaller in the north (Figure 6a). In the areas south of 38° N, the CLWC is mostly larger than 100 g·m⁻², locally reaching over 200 g·m⁻². The CLWC values in the whole snowfall areas are all over 1 g·m⁻², and their values in the areas with heavy or torrential snow (108–120° E, 38–43° N) are mainly between 10 and 100 g·m⁻². The WSM6_ORG simulation clearly underestimated the CLWC, with values of 1–10 g·m⁻² only, distributed locally in the domain (Figure 6b). The WSM6_H and WSM6_K experiments could both significantly improve the performance of CLWC simulation compared with WSM6_ORG. Like the ERA5 data, their CLWC values also show the distribution characteristic of more in the south and less in the north. There are some differences

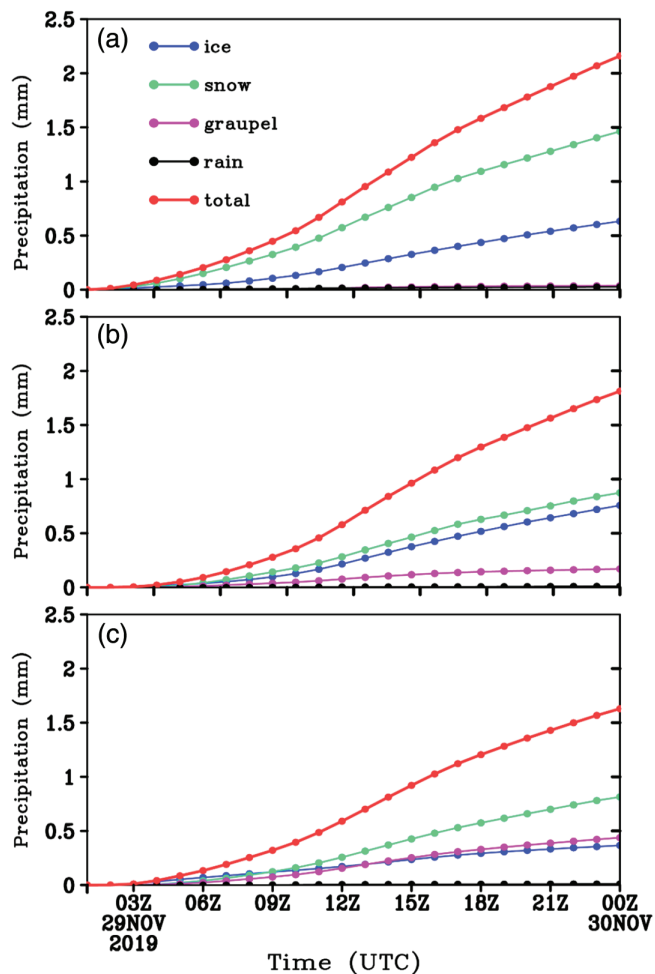


FIGURE 5 Time evolution of the ($35\text{--}50^\circ \text{N}$, $105\text{--}125^\circ \text{E}$) domain averaged accumulative precipitation (unit: mm) simulated by (a) WSM6_ORG, (b) WSM6_H, and (c) WSM6_K experiments for (black line) raindrop, (blue line) ice crystal, (green line) snow, and (pink line) graupel, and (red line) total precipitation from 0000 UTC on 29 November to 0000 UTC on November 30, 2019

in the distribution and magnitude of the CLWC simulated in WSM6_H and WSM6_K. The CLWC in WSM6_H has a smaller distribution range and lower values than that in WSM6_K. WSM6_H underestimates the CLWC in the area of $40\text{--}45^\circ \text{N}$, $118\text{--}123^\circ \text{E}$ compared with ERA5. The CLWC of WSM6_K is higher than in ERA5 data in the snowfall area.

Figures 6e-h show the distributions of the CSWC. Those with high values in the ERA5 data are consistent with the observations (Figures 4a and 6e). The CSWCs from ERA5 are almost greater than $75 \text{ g}\cdot\text{m}^{-2}$ in the entire observed snowfall area, reaching over $200 \text{ g}\cdot\text{m}^{-2}$ in the areas with high snowfall amount ($108\text{--}120^\circ \text{E}$, $38\text{--}43^\circ \text{N}$). The consistency between the CSWC and the observed snowfall indicates that the cloud product of the ERA5 data is credible and can thus be used to verify the simulated results for the NWP models. The horizontal distributions

of CSWC are well simulated in the three experiments compared with the ERA5 data. Their values are all above $50 \text{ g}\cdot\text{m}^{-2}$ in the observed snowfall area. However, the distributions of values greater than $150 \text{ g}\cdot\text{m}^{-2}$ are different due to the difference of their CLWCs. There is a competing relationship for water vapor between the simulated CSWC and CLWC in each experiment, which is related to the order of calculations for the formation of liquid and solid clouds in WSM6. The WSM6_ORG-simulated CSWC is the largest among the three experiments, while its CLWC value is the smallest (Figure 6b,f). In contrast, the WSM6_K-simulated CSWC is the smallest while its CLWC is the largest (Figure 6d,h). For instance, in the area of $113\text{--}120^\circ \text{E}$, $38\text{--}43^\circ \text{N}$, the WSM6_K-simulated CSWC is mostly between 100 and $200 \text{ g}\cdot\text{m}^{-2}$, which is the smallest, but its CLWC can be $25\text{--}100 \text{ g}\cdot\text{m}^{-2}$ and is the largest among the three experiments. The CSWC in WSM6_H is the closest one, especially for the area of CSWC exceeding $150 \text{ g}\cdot\text{m}^{-2}$.

In summary, regarding the distributions and amounts of the CLWC and CSWC, the WSM6_H experiment shows the best results consistent with ERA5 among the three experiments. The competition for water vapor at the initial formation processes of ice clouds and liquid clouds results mainly from the calculation sequence of the processes related to water vapor, as well as the specific transformation rate of the ICDS parameterizations. This is described in detail in Section 4.4 below.

Figure 7 depicts the 24-hr domain-averaged vertical profiles of the hydrometeor specific humidity in the ERA5 data and the three experiments over the snowfall area ($105\text{--}125^\circ \text{E}$, $35\text{--}47^\circ \text{N}$). The clouds in ERA5 are composed of cloud water, rain, ice, and snow. It can be seen from Figure 7a that the total hydrometeor content in ERA5 is distributed from the surface to 200 hPa, with the highest value of $0.045 \text{ g}\cdot\text{kg}^{-1}$ at 650 hPa. The vertical distributions of the total hydrometeor content simulated in the three experiments are in good general agreement with ERA5, albeit with differences in their magnitudes and constitutions between the experiments. The total hydrometeor content in WSM6_ORG is mainly from ice and snow, with almost no liquid. Their high values are mainly concentrated within 750–650 hPa, with the maximum value ($0.021 \text{ g}\cdot\text{kg}^{-1}$) around 700 hPa, located slightly lower and with much smaller magnitude than in ERA5 ($0.045 \text{ g}\cdot\text{kg}^{-1}$). Cloud water and graupel are well simulated in the WSM6_H and WSM6_K experiments. The total hydrometeors in WSM6_H and WSM6_K are composed of cloud water, ice, snow, and graupel. The maximum values of the total hydrometeor simulated by WSM6_K and WSM6_H both appear at 650 hPa, which is consistent with the distribution in ERA5. At this elevation, the total hydrometeor content in the two simulations is 0.028

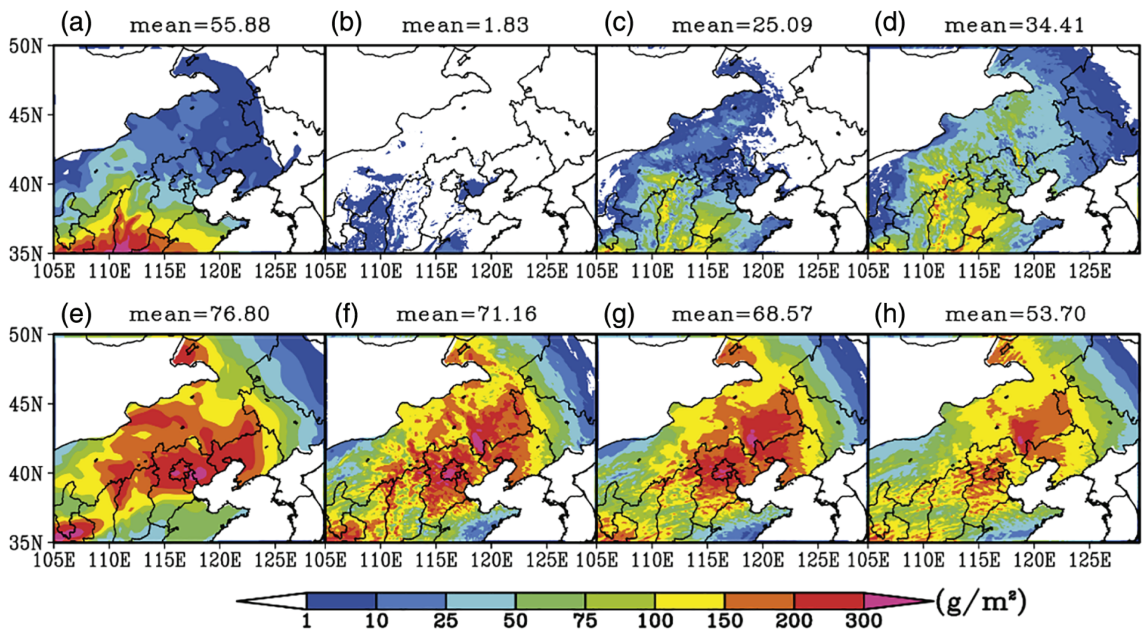
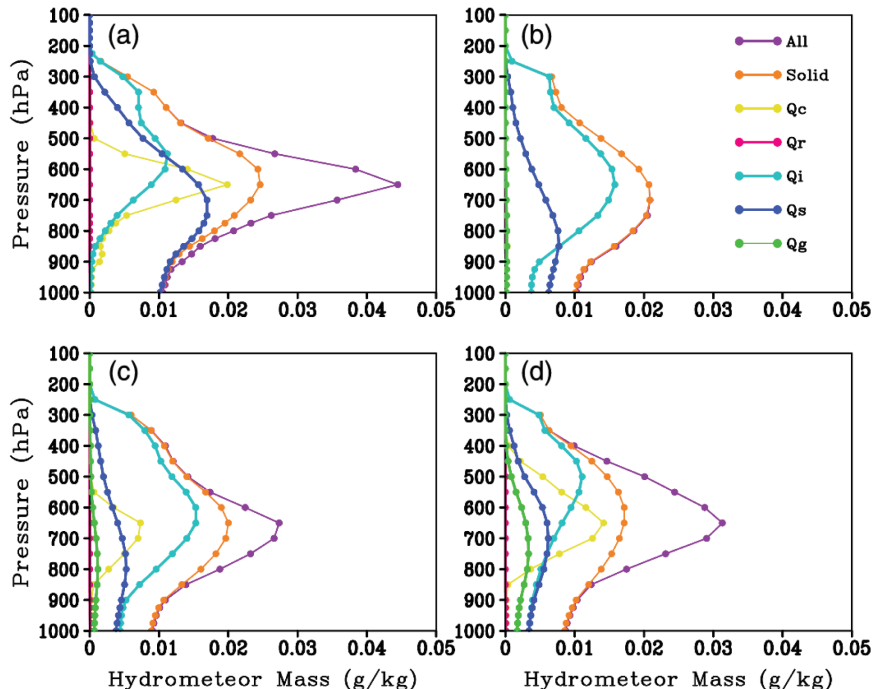


FIGURE 6 Twenty-four hour averaged (a–d) column liquid water content (CLWC) and (e–h) column solid water content (CSWC) (unit: $\text{g}\cdot\text{m}^{-2}$) from (a,e) ERA5 data and simulated by (b,f) WSM6_ORG, (c,g) WSM6_H, and (d,h) WSM6_K experiments from 0000 UTC on November 29 to 0000 UTC on November 30, 2019

FIGURE 7 Twenty-four hour domain-averaged vertical profiles of the specific humidity of hydrometeor (unit: $\text{g}\cdot\text{kg}^{-1}$) from (a) ERA5 data and simulated by (b) WSM6_ORG, (c) WSM6_H, and (d) WSM6_K experiments in the snowfall region ($105\text{--}125^\circ \text{E}, 35\text{--}47^\circ \text{N}$) from 0000 UTC on November 29 to 0000 UTC on November 30, 2019. Note that the “all” line is covered by the “solid” line in Figure 7b due to the small values of cloud water and raindrop contents in the WSM6_ORG experiment



and $0.032 \text{ g}\cdot\text{kg}^{-1}$, respectively, in better agreement with the ERA5 data than when using WSM6_ORG. In addition, it can be seen from the total hydrometeor content that the snowfall amount forecasted by WSM6_ORG is the largest, while the total hydrometeor remaining in the air is the least. In WSM6_K, the snowfall is the least while the total hydrometeor content is the greatest. The snowfall and total hydrometeor content in the WSM6_H experiment

lie between those in WSM6_ORG and WSM6_K. These differences are caused by the different ICDS parameterizations, which can lead to different conversion rates between ice-phase hydrometeor categories.

Compared with WSM6_ORG, the simulation of the supercooled cloud water is significantly improved in WSM6_H and WSM6_K. The maximum values of the cloud values from the two schemes both appear at 650 hPa,

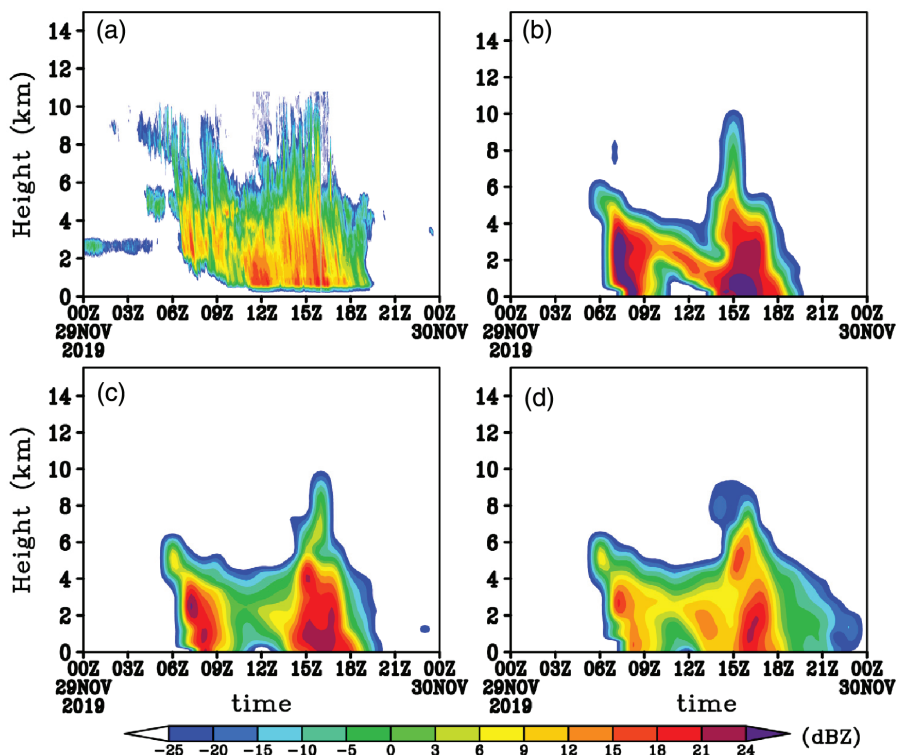


FIGURE 8 Radar reflectivity (unit: dBZ) observed from (a) MMCR and simulated by (b) WSM6_ORG, (c) WSM6_H, and (d) WSM6_K experiments at BSSAOB from 0000 UTC on November 29 to 0000 UTC on November 30, 2019

which is consistent with ERA5, with the maximum value from WSM6_K being closest. Also, the supercooled cloud water simulated by WSM6_K is mainly distributed between 850 and 400 hPa, which is a thicker layer than in ERA5. The cloud water from WSM6_H is mainly distributed between 550 and 850 hPa, with values slightly smaller than from ERA5.

For solid hydrometeors, the vertical distributions of the ice crystal category in WSM6_H and WSM6_ORG are similar. Compared with the ERA5, the vertical distributions of ice from the two schemes are over thicker layers, with ice distributed from 200 hPa to the surface. Thus, ice crystal precipitation is an important component of the total precipitation in these two experiments (Figure 5a,b). The maximum values of their mass contents both appear at 650 hPa, and are both around $0.015 \text{ g} \cdot \text{kg}^{-1}$. The ice content simulated by WSM6_K is lower than that in WSM6_H and WSM6_ORG, slightly higher than that of ERA5. The ice in the ERA5 data is mainly concentrated within 200–850 hPa, with the maximum value of $0.001 \text{ g} \cdot \text{kg}^{-1}$ at 550 hPa. Near the surface, the ice content in ERA5 data is very small, while the snow content can reach $0.01 \text{ g} \cdot \text{kg}^{-1}$, indicating that the surface precipitation in ERA5 is mainly from snow.

The snow contents near the surface in WSM6_H and WSM6_K are close to each other, with values of 0.004 and $0.0038 \text{ g} \cdot \text{kg}^{-1}$, respectively, both being smaller than the value of $0.06 \text{ g} \cdot \text{kg}^{-1}$ obtained from the WSM6_ORG simulation. The snow precipitation from the WSM6_H

and WSM6_K simulations are both lower than that in WSM6_ORG (Figure 6). In addition, unlike the WSM6_ORG, graupel particles are simulated in WSM6_H and WSM6_K. The graupel content in WSM6_K is slightly higher than that in WSM6_H. Therefore, the surface precipitation from graupel is greater in the WSM6_K than WSM6_H simulation.

Figure 8 shows the temporal evolution of the reflectivity factor observed by the MMCR at BSSAOB and simulated by the three experiments. At 0400 UTC on November 29, 2019, echoes appeared over the observation station. The echoes disappeared at 1900 UTC, and the snowfall process ended correspondingly. In this process, the highest cloud top appeared near 11 km, and the high-value echoes ($>6 \text{ dBZ}$) were mainly concentrated below 4 km, with the maximum echo reaching 18 dBZ. All three simulations capture the initiation time of the snowfall echoes. The near-ground echoes all appeared at around 0600 UTC, which is consistent with the observations. The dissipation time of the snowfall process simulated by WSM6_ORG and WSM6_H is in good agreement with the observations (at about 2000 UTC). In contrast, the dissipation time given by WSM6_K is later than in the observations, and there were still some weak echoes from 2000 to 2300 UTC. The highest echo tops in the three experiments all appear near 10 km, slightly lower than observed by MMCR. During the 0900–1400 UTC period, the echo tops in WSM6_H and WSM6_K are higher than that in WSM6_ORG, and they are more consistent with the observations. The

echo intensity simulated by WSM6_ORG is significantly stronger than the observations, and the maximum values appear from 0600 to 0900 UTC and from 1300 to 1800 UTC, with the echoes locally exceeding 24 dBZ. The reflectivity simulated by WSM6_H is significantly weaker than that in WSM6_ORG during these two periods, with the values below 24 dBZ. The maximum value in WSM6_K is smaller, and the distribution is relatively uniform and continuous. Compared with WSM6_ORG, WSM6_K and WSM6_H simulated better values of the radar reflectivity, the intensity and distribution of which are closer to the observations of MMCR. The near-surface reflectivity values simulated by the two experiments are weaker than that from WSM6_ORG, indicating the lower hydrometeor content. Hence, the precipitation amounts from the two experiments are also lower than that in WSM6_ORG. This is consistent with the conclusions in Section 4.1 (Figures 4 and 5).

4.4 | Microphysical budget

The transformation characteristics of the microphysical processes involving water vapor in WSM6 are analyzed to evaluate the different ICDS parameterizations. The impacts of different ICDS parameterization schemes on other transformation processes are also investigated through the microphysical budget analysis. To understand this point better, the processing and calling sequence of the water vapor-related microphysical processes in the WSM6 scheme are introduced below.

In WSM6, the water vapor-related transformation processes include the condensation and evaporation of cloud water (*ccond/cevap*) and rain (*rcond/revap*), deposition/sublimation of ice, snow, and graupel (*idep/isub*, *sdep/ssub*, *gdep/gsub*), and ice nucleation (*pvi*). These processes are calculated and updated in the order shown in Figure 9. The condensation (deposition) process is illustrated as an example. In WSM6, the *rcond* process in the warm region ($T > 0^\circ\text{C}$) is calculated first when the water vapor is supersaturated over liquid surface. In the cold region, the conversion rates of *idep*, *sdep*, *gdep*, and *pvi* are calculated sequentially. Before calculating the ice-phase processes, the maximum depositable rate of water vapor (*Satdt*) at the grid in this time step is calculated. In the serial calculation, the conversion rate of the process is subtracted from the total deposition rate (i.e., *Satdt* – *idep*) after each calculation. When the total depositable rate is insufficient (*ifsat* = .False.), the other conversion processes that follow will not be calculated. Under this calculation sequence and restriction conditions, it can be ensured that, in the calculating processes, the total deposition rate does not exceed the maximum depositable rate in this time step. At

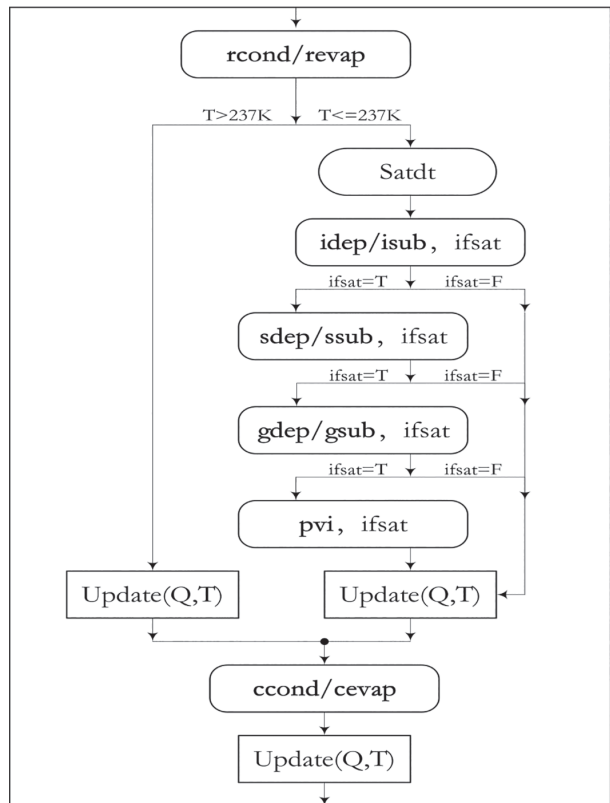


FIGURE 9 Flowchart of the microphysical processes related to water vapor in WSM6. The symbols are shown in the Appendix

the same time, as the water vapor is the most sufficient in the first calculated deposition process, the conversion rate of the following processes will definitely be affected if the rate calculated in the *idep* process is too large.

After the above calculations related to the water vapor, the changes in the temperature, water vapor, and hydrometeor mixing ratios are updated separately in the cold and warm sections. Then, *ccond* is calculated and its tendency updated. Obviously, for this calculation order, when the air temperature is below 0°C , the temperature and water vapor at the grid reach equilibrium according to the saturation specific humidity over ice surface after the tendency update due to the ice-phase processes. Because the saturation specific humidity over liquid is greater than that over ice, it is difficult for cloud water to condense, or it may even evaporate when *ccond* is calculated under this condition. Therefore, the calculation sequence and update manner of the vapor-related processes in WSM6 could hinder condensation of cloud water in the cold region and even tend to make it evaporate. Moreover, if too much water vapor is consumed in the ice phase and the specific humidity of the updated water vapor is not greater than the saturation specific humidity over the liquid surface, evaporation will occur in the cold region, resulting in less supercooled cloud water. Condensation in the cold region will only

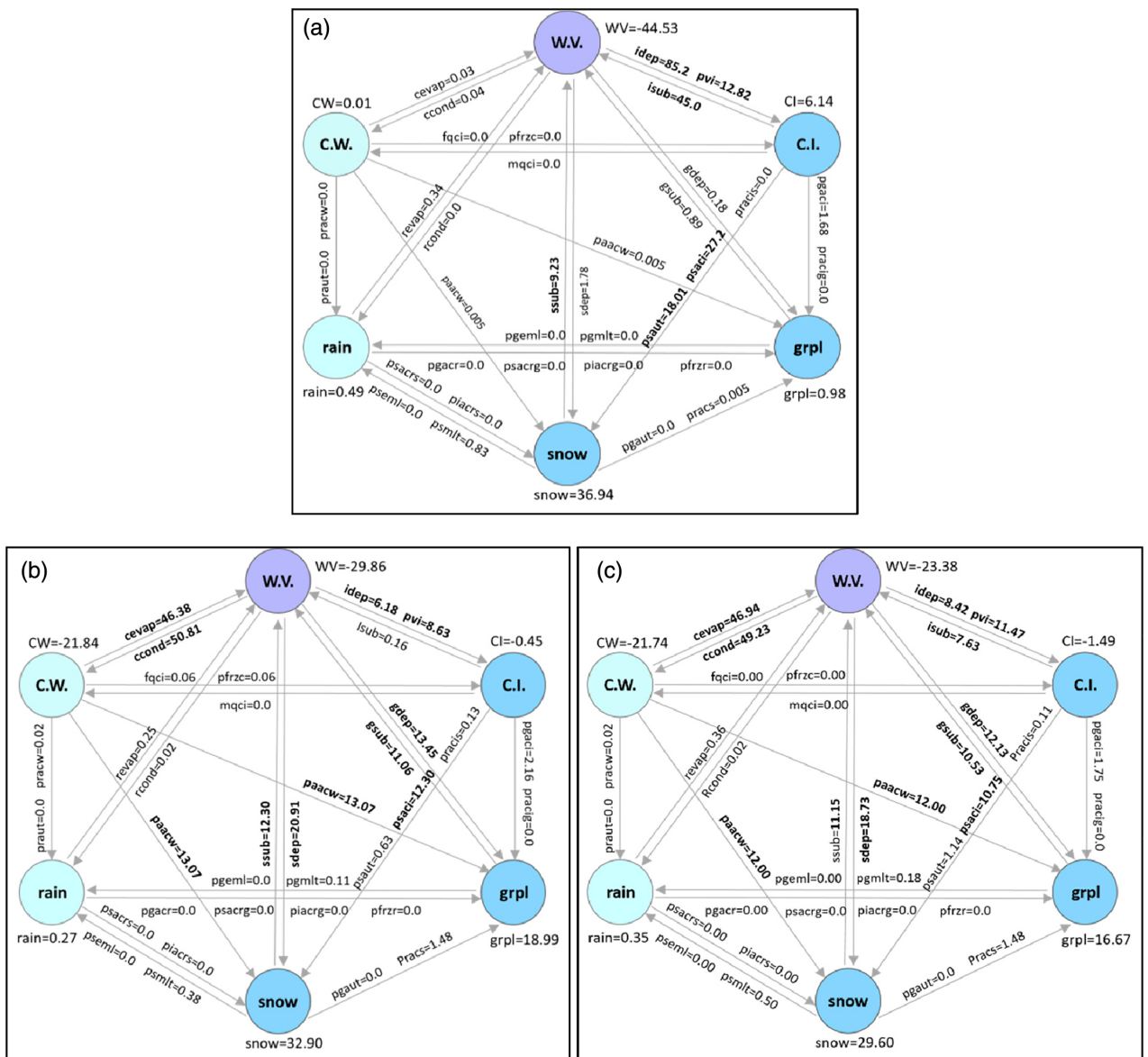


FIGURE 10 (a) Flowchart of the microphysical processes averaged between 6 and 18 hr for three WSM6_ORG experiments. The circles denote the various water species (water vapor, cloud water, ice crystal, rain, snow, and graupel), while the arrows indicate the processes that link the two species in the WSM6 scheme (see Appendix for a list of all processes). The values shown are the ratio of each microphysical process rate to the total sink terms of water vapor WVL ($ccond + rcond + pvi + idep + sdep$) in the WSM6 scheme within the box. The sum of all the microphysical process tendencies for each species is given by (WV, CW, rain, CI, snow, and grpl), which does not include horizontal advection, diffusion/divergence, and sedimentation. Microphysical processes above 5% of the WVL rate are in bold. (b) and (c) same as (a), but for WSM6_H and WSM6_K, respectively [Colour figure can be viewed at wileyonlinelibrary.com]

occur if the specific humidity remains higher than the saturation with respect to water after all the ice-phase processes.

Figure 10 shows the microphysical processes averaged horizontally and vertically within the domain 108–120° E and 38–43° N between 0600 and 1800 hr for the three experiments. The ice-phase cloud microphysical transformation processes in WSM6_ORG are mainly *idep* and *pvi* processes, which account for 98.02% of water vapor loss (WVL). Among them, the proportion of *idep* (85.2%) is

the largest. The deposition rates of snow and graupel are very small, accounting for only 1.78% and 0.18%, respectively. The sublimation is similar; the $isub$ is the most intense, with a rate of 45.0%, and the $ssub$ rate is 9.23%. The $gsub$ rate is only 0.89%. The growth process of the ice-phase cloud particles in WSM6_ORG is dominated by the conversion (aggregation) of ice to snow ($Psaut$) and the accretion of cloud ice by snow ($Psaci$). The normalized values of these processes are 18.01% and 27.2%, respectively. The growth of graupel is relatively weak. In the

graupel-related microphysical processes, the accretion of cloud ice by graupel (*Pgaci*) is the most significant, while its normalized value is only 1.68%; those in other processes are less than 1.0%. For the liquid-phase clouds, the condensation and evaporation processes of cloud rain in WSM6_ORG are both very weak.

The microphysical conversion rates in WSM6 are very sensitive to the ICDS parameterizations. As can be seen from Figure 10b,c, the *idep* rates in WSM6_H and WSM6_K are weaker than that in WSM6_ORG, with the *idep* rates decreasing to 6.18% and 8.42%, respectively. This is consistent with the *idep* value (3.94%) obtained in the analysis of a snowfall process in winter by Colle *et al.* (2005). Due to the lower consumption of vapor in *idep*, the *sdep* and *gdep* rates in both WSM6_H and WSM6_K are notably enhanced. The *sdep* rates in WSM6_H and WSM6_K increase from 1.78% in WSM6_ORG to 20.91% and 18.73%, respectively. Meanwhile, *gdep* increases from 0.18% to 13.45% and 12.13%, respectively. There are no significant differences in the *pvi* rates between the two experiments and WSM6_ORG. When the *idep* parameterization is changed, the transformation rate from ice to snow is decreased due to the lower ice mass content. In WSM6_H and WSM6_K, the rates of conversion (aggregation) from ice to snow (*Psaut*) decrease from 18.01% in WSM6_ORG to 0.63% and 1.14%, respectively. Meanwhile, the rates of accretion of cloud ice by snow (*Psaci*) also decrease.

The *ccond* (*cevap*) processes in WSM6_H and WSM6_K also exhibit significant changes. Compared with WSM6_ORG, *cevap* and *ccond* are both enhanced. Their normalized condensation rates are 50.81% and 49.23%, and the evaporation rates are 46.38% and 46.94%, respectively. The enhancement of *ccond* results from the reduction of water vapor consumption in the ice-phase processes after adopting the ICDS parameterization schemes. The proportion of the total water vapor consumption in the ice-phase deposition processes (*idep* + *sdep* + *gdep* + *pvi*) decreases from 99.98% in WSM6_ORG to 49.17% and 50.75% in WSM6_H and WSM6_K, respectively. In this way, there will be more water vapor remaining for *ccond*. Due to the increase of the supercooled cloud water, the cloud water-related processes are more active in the two experiments. For example, the conversion rate of the accretion of cloud water by snow/graupel (*paacw*) increases from a very small value in WSM6_ORG to 13.07% and 12.0% in WSM6_H and WSM6_K, respectively. Supercooled cloud water is transformed into solid hydrometeors through accretion.

In WSM6_H and WSM6_K, ice crystal decreases because of the reduction of *idep*. The growth of snow is determined by the *idep*, *paacw*, and *pacci*, which are dominated by *psaut* and *psaci* in WSM6_ORG. The rates of *psaut*

decrease from 18.01% to 0.63% and 1.14%, respectively. In the two experiments, the growth of graupel is mainly due to *gdep* and *paacw*. In contrast, these two processes are very weak in WSM6_ORG. Therefore, the graupel content and its contribution to snowfall in WSM6_H and WSM6_K both increase significantly compared with WSM6_ORG (Figure 5). The vapor loss is reduced from 44.53 kg·m⁻² in WSM6_ORG to 29.86 kg·m⁻² and 23.38 kg·m⁻² in WSM6_H and WSM6_K, respectively, which is consistent with the changes of their simulated snowfall amount.

Figure 11 shows the horizontally and temporally averaged (from 1–24 hr) tendency profiles of the water vapor-related microphysical processes in the snowfall area (105–125° E, 35–47° N) in the three experiments. Figure 11a shows the profiles of *idep* and *isub*. It can be seen that the vertical range (below 9 km) and magnitude of *idep* simulated by WSM6_ORG are both significantly larger than in WSM6_H and WSM6_K. The maximum conversion rate is located at a height of 1.8 km, reaching 0.38 g·kg⁻¹·day⁻¹. The vertical range of *idep* in WSM6_H is slightly narrower than that in WSM6_ORG. The vertical distribution characteristics of *idep* in WSM6_K are different from those in WSM6_ORG and WSM6_H. It is mainly distributed between 5 and 10 km. The maximum conversion rate appears near 6.5 km, being only 0.14 g·kg⁻¹·day⁻¹. The *isub* in the three experiments show similar characteristics to *idep*. The maximum of *isub* in WSM6_ORG appears in the low levels, which may be related to the fact that ice crystal falls out of the cloud bottom and there are more occurrences of *isub*. The range of sublimation rate in WSM6_H is almost the same as that in WSM6_ORG, but its magnitude is smaller, with the maximum value being 0.16 g·kg⁻¹·day⁻¹. For the net deposition and sublimation (*idep* + *isub*), the net deposition appears within 1–6.5 km in WSM6_ORG and WSM6_H, and the net sublimation appears below 1 km and within 6.5–9 km, respectively. They differ mainly in intensity. For example, the maximum net deposition in WSM6_ORG is 0.22 g·kg⁻¹·day⁻¹, nearly twice as much as the value of 0.13 g·kg⁻¹·day⁻¹ in WSM6_H. This is the main reason for the difference between their relative humidity fields (Figure 3b,c). The net deposition and sublimation in WSM6_K is mainly distributed from 5 to 10 km. The net deposition processes appear in all the layers except around 8 km.

Competition for water vapor exists in the WSM6 scheme due to the serial calculation of the process rates. Figure 11b illustrates the obvious change of the *sdep* (*ssub*) process due to the different intensity of the *idep* (*isub*) in WSM6. Because of the strong *idep* process in WSM6_ORG, *sdep* is very weak, with most values close to 0. In WSM6_H, nonzero *sdep* values occur from 1 to 9 km and the values are all smaller than 0.015 g·kg⁻¹·day⁻¹. Due to the

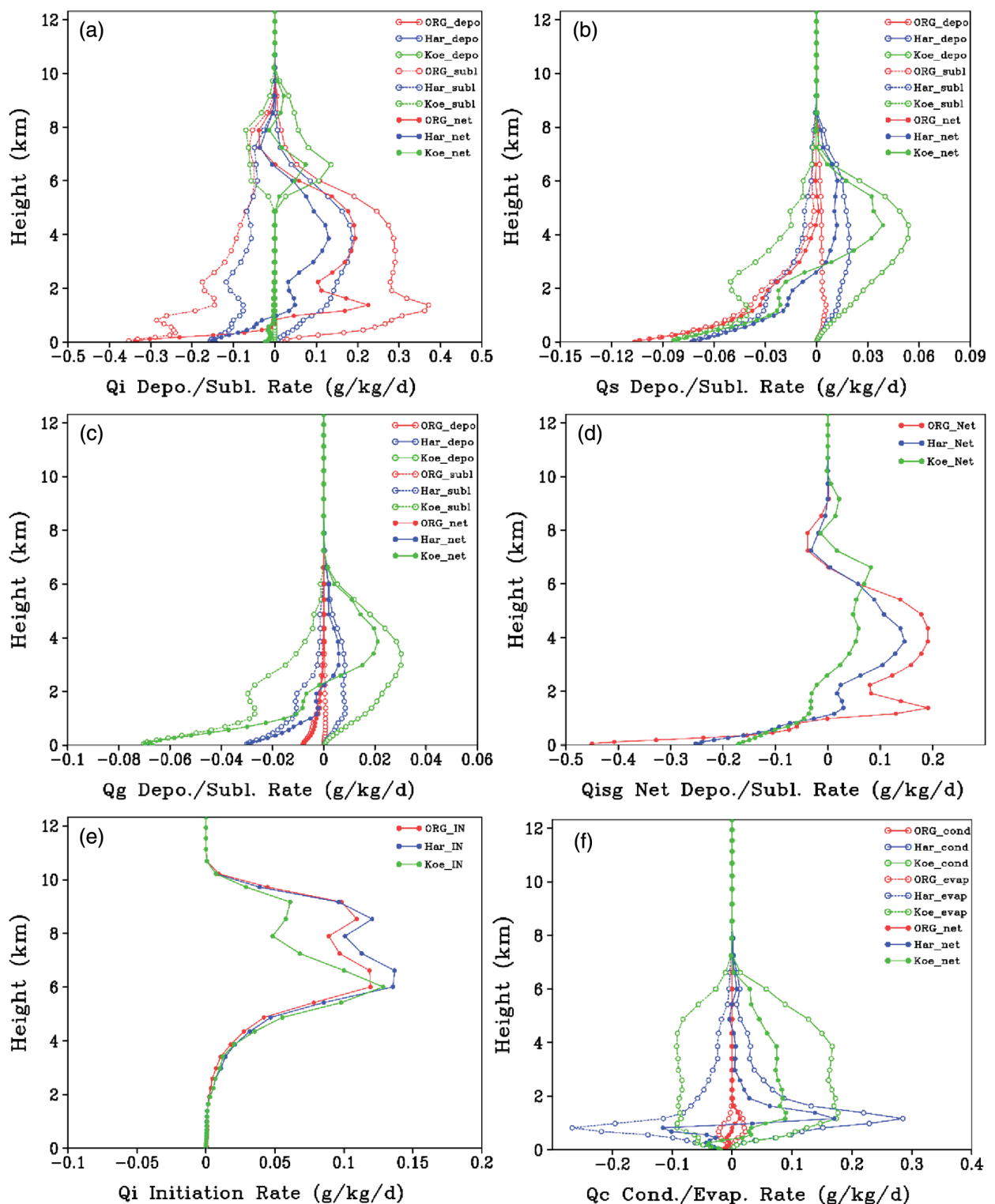


FIGURE 11 Horizontally and temporally averaged (from 1 to 24 hr) tendency profile of microphysics processes related to water vapor (unit: $\text{g} \cdot \text{kg}^{-1} \cdot \text{day}^{-1}$) in the snowfall domain (105–125° E, 35–47° N): (a) deposition/sublimation of ice crystal, (b) deposition/sublimation of snow, (c) deposition/sublimation of graupel, (d) total net deposition and sublimation of ice crystal, snow, and graupel, and (e) initiation nucleation of ice crystal, and (f) condensation/evaporation of cloud water. Red, blue, and green lines denote the WSM6_ORG, WSM6_H, and WSM6_K experiment, respectively. The solid line with hollow circle and the dotted line with hollow circle represent condensation/deposition process and its reverse process (evaporation/sublimation), respectively. The solid line with solid circle denotes the net value for each process of the corresponding experiment. Note that the x axis scales are different among the plots

relatively weak *idep* rates, *sdep* and *ssub* in WSM6_K are both the greatest among the three simulations. For the net deposition and sublimation of snow, *ssub* dominates below 8.5 km in WSM6_ORG due to the low *sdep*. The *sdep* is dominant from 2.5 to 7.5 km in both WSM6_H and WSM6_K. The net deposition and sublimation amount of snow in WSM6_K is greater than that in WSM6_H. Below 2.5 km, the *ssub* processes dominate in both experiments, with similar values. The strength of the *gdep* (*gsub*) process is also affected by the ICDS parameterization, and the deposition (sublimation) conversion rate of graupel is more obviously impacted by the *idep* parameterization than that of snow (Figure 11c). As *idep* (*isub*) in WSM6_ORG is the strongest among the three experiments, the deposition rate, sublimation rate, and net deposition rate of graupel in WSM6_ORG are all the smallest. However, as *idep* is very small below 6.5 km in WSM6_K, the corresponding transformation between graupel and water vapor is the most intense.

The total net deposition and sublimation rate of all ice-phase categories (ice + snow + graupel) from the WSM6_ORG below 6 km is the largest among the three experiments, while that of WSM6_K is the smallest (Figure 11d). At heights 6.5–10 km, it is the net deposition in WSM6_K, while it is the net sublimation in WSM6_ORG and WSM6_H. This difference is fully caused by the difference in the *idep* (*isub*) process. Since the *pvi* process is at the end of the serial calculation, the *pvi* is affected by the total net deposition and sublimation of ice, snow, and graupel (Figure 11e). The *pvi* differences among the three experiments mainly appear at heights of 6–10 km. As the processes are dominated by net deposition in WSM6_K, its *pvi* rate is the lowest. However, at elevations of 6–10 km in WMS6_ORG and WSM6_H, the processes for ice, snow, and graupel are dominated by sublimation, so the *pvi* processes in these two experiments are stronger than that in WSM6_K.

The competition for water vapor between the *ccond* process and the ice-phase processes also exists in the WSM6 scheme, which is well illustrated in Figure 11f. In WSM6_ORG, ice-phase deposition accounts for the most water vapor, so *ccond* is the smallest among the three experiments, and only occurs below 2 km with a rate of only $0.02 \text{ g}\cdot\text{kg}^{-1}\cdot\text{day}^{-1}$. Below 6 km, the water vapor consumed by the ice-phase deposition process in WSM6_K is the least, and more water vapor is left for *ccond*. Therefore, *ccond* is the largest in WSM6_K. From Figure 6d, larger CLWC is found in the WSM6_K simulation. Near 1 km, the WSM6_H has the largest condensation rate ($0.28 \text{ g}\cdot\text{kg}^{-1}\cdot\text{day}^{-1}$) among the three experiments; however, *ccond* in WSM6_H at most of the other heights lies between the values in WSM6_ORG and WSM6_K. Similarly, *cevap* and the net condensation in the three experiments have similar characteristics.

4.5 | Batch experimental verification

To analyze further the impact on the simulated snowfall of using the Harrington and Koenig ICDS parameterizations in the WSM6 scheme, six snowfall processes with eight snowfall days in the analysis area that occurred from November 2019 to February 2020 are selected for batch simulations. The improvement in the forecast for each snowfall case due to the different ICDS parameterizations is analyzed through the Taylor diagram.

Table 2 shows the occurrence time, snowfall coverage, number of stations, maximum precipitation, and mean precipitation for the eight snowfall cases. The regional averaged snowfall amounts of cases 2 and 3 reach the level of moderate snow (2.5–5 mm). The maximum precipitation observed at the two stations is 13.8 and 18.7 mm, respectively. The regional averaged snowfall amounts for the other six cases all correspond to light snow.

TABLE 2 The information for six snowfall cases with eight snowfall days in winter 2019

Serial number	Observation time	Snowfall domain	Stations number	Maximum precipitation (mm)	Mean precipitation (mm)
1	2,019,113,000	110–125 37–47	297	11.7	2.34
2	2,019,121,600	105–125 37–45	383	13.8	2.58
3	2,020,010,600	105–125 37–47	378	18.7	4.62
4	2,020,011,700	105–120 35–45	132	3.10	0.69
5	2,020,020,200	105–122 35–45	281	8.40	1.61
6	2,020,020,300	115–125 37–44	133	3.80	0.90
7	2,020,020,600	112–120 35–42	190	6.20	1.11
8	2,020,020,700	112–120 35–42	174	1.60	0.39

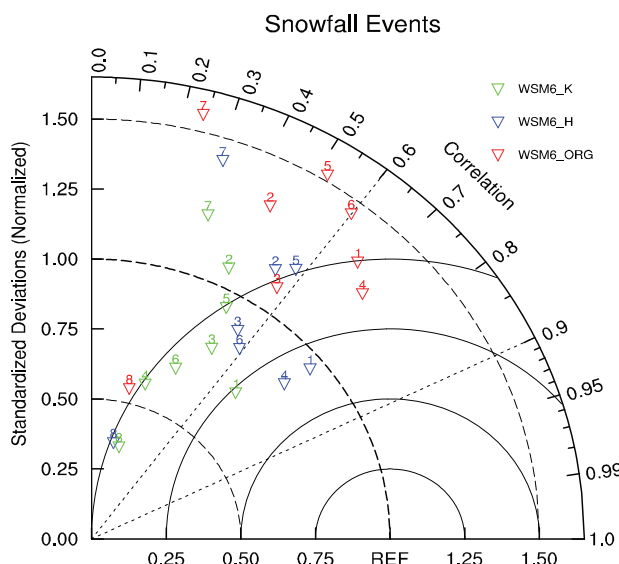


FIGURE 12 Taylor verification for all eight snowfall days simulated by WSM6_ORG, WSM6_H, and WSM6_K

The Taylor diagram (Figure 12) shows the correlation coefficients (CC) and the standardized standard deviations (SSD) between the simulated and observed snowfall in all cases. The closer the SSD is to 1, the smaller the deviation between simulation and observation and the better the modeling performance. As shown in Figure 12, the SSDs in WSM6_ORG are greater than 1 for all cases except case 8, and the SSDs of cases 5 and case 7 are even greater than 1.5, indicating that systematic overestimation exists in most snowfall processes in WSM6_ORG. The SSDs in WSM6_H and WSM6_K are both smaller than in WSM6_ORG, showing that the precipitation simulated by the two configurations is generally smaller than that in WSM6_ORG. For the WSM6_H experiment, except for case 8 (SSD further away from 1) and case 3 (equivalent distance with 1), the SSDs of the other six cases are closer to 1 than those in WSM6_ORG. The SSDs of five cases among them are between 0.75 and 1.25, revealing that the snowfall amount in WSM6_H is closer to the observations. The snowfall forecasted by WSM6_K is the weakest. Except for cases 2 and 7, the SSDs of other cases are all less than 1, indicating that WSM6_K underestimates the snowfall. This is consistent with the conclusions in the case analysis (Figure 4c). Compared with WSM6_ORG, the SSDs of five cases (1, 2, 5, 6, and 7) simulated by WSM6_K are closer to 1, while the SSDs of the other three cases (3, 4, and 8) are farther from 1 than those in WSM6_ORG.

We next analyze the CC between the model simulations and observations, noting that, the closer the CC is to 1, the better the simulation overall. For WSM6_H, the CC of five cases (1, 2, 5, 7, and 8) are better than those in WSM6_ORG, while the CC of the other three cases (3, 4, and 6) are equivalent to those in WSM6_ORG. In

WSM6_K, the CC of case 7 is slightly better than that in WSM6_ORG. The CCs of three cases (1, 5, and 8) are equivalent to those in WSM6_ORG, while those of the other four cases (2, 3, 4, and 6) are slightly worse. The poor performance on case 7 is related to both the overestimation of the range of precipitation (small CC) and the amount (large SSD; not shown) by all three scheme configurations.

In summary, in terms of the CCs and SSDs of all the cases, the WSM6_H experiment outperforms WSM6_ORG. The overestimation of the snowfall in the original scheme is reduced in WSM6_H, and the CCs with the observations are also the highest in WSM6_H. For most cases, the SSDs in WSM6_K are less than 1, and the CCs with the observations are also lower than in WSM6_H and WSM6_ORG. Therefore, the improvement of the WSM6_K scheme on snowfall is not satisfactory.

5 | CONCLUSIONS AND DISCUSSION

Overestimation of snow precipitation is common in operational numerical weather forecasts from the GRHRDPS of the NWPC/CMA. This includes the snowfall case in North China on November 29–30, 2019. This is an urgent problem to be solved for meteorological support for the upcoming 2022 Beijing Winter Olympic Games. Since the convective parameterization scheme is not used in GRHRDPS, aspects of the WSM6 cloud microphysics scheme are possible reasons for the overestimation of snowfall. The water-vapor-related transformation process in the cloud microphysical schemes is the only source for the generation of cloud and precipitation. Therefore, this study mainly focused on the microphysical transformation characteristics related to the water vapor in the WSM6 scheme. Two alternative ICDS parameterization schemes, proposed by Harrington *et al.* (1995) and Koenig (1972), were implemented into WSM6 to carry out the sensitivity experiments. Through the comparison with the ERA5 reanalysis data, the MMCR data and the gauge precipitation data, the impacts of cloud microphysical schemes on the forecast of hydrometeors, microphysical transformation rates related with water vapor, and precipitation during this snowfall episode were investigated. To strengthen the conclusions, batch simulations and analyses on eight snowfall days from November 2019 to February 2020 are carried out to evaluate the improvement of snowfall forecast when using the two ICDS parameterizations in WSM6. The main conclusions are as follows.

1. The simulation results of the snowfall case show that the simulation of snowfall quantity using WSM6 is very sensitive to the ICDS parameterization. The

- snowfall due to this process is significantly overestimated in WSM6_ORG. The overestimation is notably reduced in the WSM6_H and WSM6_K experiments, with the amount simulated by WSM6_H being closest to the observations. The snowfall amount simulated by WSM6_K is less than the observations in the area with large snowfall amount. The snowfall simulated by WSM6_ORG comes from the precipitation of ice crystals and snow, while in WSM6_H and WSM6_K it comes from a combination of ice, snow, and graupel. The graupel sedimentation generates more precipitation in the WSM6_K experiment.
2. Compared with the ERA5 reanalysis, the underestimation of supercooled liquid water content in WSM6_ORG is reduced in WSM6_H and WSM6_K. The WSM6_K experiment produces more supercooled liquid water than WSM6_H. At the same time, the CSWCs in the two experiments decrease correspondingly. The CSWC simulated in WSM6_H is in better accordance with that in the ERA5 data. The vertical distributions and intensities of radar reflectivities simulated by WSM6_H and WSM6_K are more consistent with the MMCR observations than those in WSM6_ORG, but the echo duration in WSM6_K is slightly longer than the observation.
 3. Due to the calculation and tendency updating sequences of the water-vapor-related transformation processes in the WSM6 cloud scheme, there is competition for water vapor among *idep*, *sdep*, and *gdep*, as well as between the processes of ice-phase deposition and *ccond*. In addition, updating the tendencies of ice-phase microphysical processes before calculating *ccond* hinders its occurrence in cold regions and may even lead to evaporation. In WSM6_ORG, as *idep* (*isub*) is too strong, the *sdep*, *gdep*, and *ccond* values are very weak in cold regions. This is the main reason for the underestimation of supercooled water in WSM6. In both WSM6_H and WSM6_K, the *idep* values are less than that in WSM6_ORG, thus the rates given by *sdep*, *gdep*, and *ccond* are enhanced. At the same time, other related microphysical transformation processes become more active, and the proportion of precipitation from graupel increases.
 4. The Taylor diagram is used to analyze the simulation results of eight snowfall days that occurred from November 2019 to February 2020. The overestimation of snowfall in WSM6_ORG is reduced in the WSM6_H. With a smaller standard deviation and a higher correlation coefficient with the station observations, the WSM6_H scheme improves the snowfall forecast performance in the GRAPES regional operation model. Overall, the SSD and the correlation coefficient in

the WSM6_K experiment are inferior to those in the WSM6_H and WSM6_ORG experiments.

5. Based on our experimental results, there are still large differences and uncertainties between the ICDS parameterizations, which affect the formation of ice clouds, especially for snowfall in winter. In addition, the treatments of the microphysics processes related with water vapor are very important in cloud microphysics schemes because of the competition for water vapor. The calculations and update orders of the condensation/evaporation, deposition/sublimation processes could impact on the content of each hydrometeor species, and even the precipitation.

Carrying out sensitivity experiments of snowfall cases in winter makes it possible to diagnose possible problems in the parameterized ice-phase processes in cloud microphysics schemes. In this study, the improvements in the simulations of hydrometeor content and snowfall amount were analyzed from the perspective of ICSD parameterizations. This study also focused on the potential influence of the calculation and updating sequence of water-vapor-related processes in the WSM6 scheme. Although the focus of this study is on snow precipitation, it should be recognized that a considerable amount of rainfall originates from melting snow, particularly for stratiform cases. Therefore, it would be reasonable to expect that the choice of ICSD parameterization in WSM6 would have a significant impact on numerical precipitation forecasts in GRHRDPS in all seasons.

ACKNOWLEDGEMENTS

The authors thank the entire GRAPES team for their support with this work. We also gratefully acknowledge the Nanjing Hurricane Translation for reviewing the English-language quality of this article. This study was supported by the National Key R&D Program on Monitoring, Early Waring and Prevention of Major Natural Disasters (grants 2017YFC1501406, 2017YFC1502001, and 2018YFC1505702), the National Key R&D program on Global Change and Response (grant 2019YFA0606803), the National Natural Science Foundation of China (grants 42090032, 42075155, and 41925022), and the State Key Laboratory of Earth Surface Processes and Resource Ecology.

CONFLICT OF INTEREST

The authors declare that they have no conflicts of interest.

AUTHOR CONTRIBUTIONS

Zhanshan Ma: Conceptualization; data curation; formal analysis; methodology; resources; validation;

visualization; writing - original draft. **Jason Milbrandt:** Formal analysis; investigation; supervision; writing-review & editing. **Qijun Liu:** Formal analysis; funding acquisition; investigation; resources. **Chuanfeng Zhao:** Conceptualization; formal analysis; funding acquisition; investigation; project administration; supervision; writing-review & editing. **zhe li:** Formal analysis; validation; visualization. **Fa Tao:** Formal analysis; investigation; methodology. **Jian Sun:** Formal analysis; funding acquisition; investigation; supervision; validation. **Xueshun Shen:** Funding acquisition; investigation; resources; supervision; writing-review & editing. **Qi Kong:** Data curation; formal analysis. **Feifei Zhou:** Data curation; formal analysis. **Liping Huang:** Formal analysis. **Dai Kan:** Formal analysis. **Leqiang Sun:** Formal analysis. **Jiong Chen:** Formal analysis. **Qingu Jiang:** Data curation; formal analysis. **Hao Fan:** Formal analysis. **Yikun Yang:** Formal analysis. **Xiangfeng Hu:** Formal analysis; validation.

ORCID

Chuanfeng Zhao  <https://orcid.org/0000-0002-5196-3996>

Zhe Li  <https://orcid.org/0000-0002-2547-7185>

Jiong Chen  <https://orcid.org/0000-0002-7010-7570>

REFERENCES

- Abramovitz, M. and Stegun, I.A. (1972) *Handbook of Mathematical Functions*. Mineola, NY: Dover, p. 1046.
- Ahlgrimm, M. and Forbes, R. (2014) Improving the representation of low clouds and drizzle in the ECMWF model based on ARM observations from the Azores. *Monthly Weather Review*, 142(2), 668–685.
- Aligo, E.A. (2011) *An evaluation of fall speed characteristics in bin and bulk microphysical schemes and use of bin fall speeds to improve forecasts of warm-season rainfall*. Graduate Thesis and Dissertations, Iowa State University, p. 195.
- Barszcz, A., Milbrandt, J.A. and Thériault, J.M. (2018) Improving the explicit prediction of freezing rain in a kilometer-scale numerical weather prediction model. *Weather and Forecasting*, 33, 767–782.
- Bauer, P., Thorpe, A. and Brunet, G. (2015) The quiet revolution of numerical weather prediction. *Nature*, 525, 47–55.
- Byers, H.R. (1965) *Elements of Cloud Physics*. Chicago, IL: The University of Chicago Press, p. 191.
- Chen, F. and Dudhia, J. (2001) Coupling an advanced land surface-hydrology model with the Penn State-NCAR MM5 modeling system. Part I: model implementation and sensitivity. *Monthly Weather Review*, 129, 569–585.
- Chen, J., Ma, Z., Li, Z., Shen, X., Su, Y., Chen, Q. and Liu, Y. (2020) Vertical diffusion and cloud scheme coupling to the Charney-Phillips vertical grid in GRAPES global forecast system. *Quarterly Journal of the Royal Meteorological Society*, 146, 2191–2204.
- Chen, Q., Shen, X., Sun, J. and Liu, K. (2016a) Momentum budget diagnosis and the parameterization of subgrid-scale orographic drag in global GRAPES. *Journal of Meteorological Research*, 30, 771–788.
- Chen, T., Guo, J., Li, Z., Zhao, C., Liu, H., Cribb, M., Wang, F. and He, J. (2016b) A CloudSat perspective on the cloud climatology and its association with aerosol perturbations in the vertical over eastern China. *Journal of the Atmospheric Sciences*, 73, 3599–3616.
- Cintineo, R., Otkin, J.A., Xue, M. and Kong, F. (2014) Evaluating the performance of planetary boundary layer and cloud microphysical parameterization schemes in convection-permitting ensemble forecasts using synthetic GOES-13 satellite observations. *Monthly Weather Review*, 142, 163–182.
- Colle, B.A., Garvert, M.F., Wolfe, J.B., Mass, C.F. and Woods, C.P. (2005) The 13–14 December 2001 IMPROVE-2 event. Part III: simulated microphysical budgets and sensitivity studies. *Journal of the Atmospheric Sciences*, 62, 3535–3558.
- Colle, B.A. and Zeng, Y. (2004a) Bulk microphysical sensitivities within the MM5 for orographic precipitation. Part I: the Sierra 1986 event. *Monthly Weather Review*, 132, 2780–2801.
- Colle, B.A. and Zeng, Y. (2004b) Bulk microphysical sensitivities within the MM5 for orographic precipitation. Part II: impact of barrier width and freezing level. *Monthly Weather Review*, 132, 2802–2815.
- Comin, A.N., Schumacher, V., Justino, F. and Fernández, A. (2018) Impact of different microphysical parameterizations on extreme snowfall events in the southern Andes. *Weather and Climate Extremes*, 21, 65–75.
- Dee, D.P., Uppala, S.M., Simmons, A.J., Berrisford, P., Poli, P., Kobayashi, S., Andrae, U., Balmaseda, M.A., Balsamo, G., Bauer, P., Bechtold, P., Beljaars, A.C.M., van de Berg, L., Bidlot, J., Bormann, N., Delsol, C., Dragani, R., Fuentes, M., Geer, A.J., Haimberger, L., Healy, S.B., Hersbach, H., Holm, E.V., Isaksen, L., Källberg, P., Köhler, M., Matricardi, M., McNally, A.P., Monge-Sanz, B.M., Morcrette, J.-J., Park, B.-K., Peubey, C., de Rosnay, P., Tavolato, C., Thépaut, J.-N. and Vitart, F. (2011) The ERA-interim reanalysis: configuration and performance of the data assimilation system. *Quarterly Journal of the Royal Meteorological Society*, 137, 553–597.
- Dudhia, J. (1989) Numerical study of convection observed during the winter monsoon experiment using a mesoscale two-dimensional model. *Journal of the Atmospheric Sciences*, 46(20), 3077–3107.
- Dudhia, J. (1993) A nonhydrostatic version of the Penn State-NCAR mesoscale model: validation tests and simulation of an Atlantic cyclone and cold front. *Monthly Weather Review*, 121, 1493–1513.
- Fernández-González, S., Valero, F., Sánchez, J.L., Gascón, E., López, L., García-Ortega, E. and Merino, A. (2015) Numerical simulations of snowfall events: sensitivity analysis of physical parameterizations. *Journal Geophysical Research: Atmospheres*, 120, 10130–10148.
- Forbes, R., Tompkins, A.M. and Untch, A. (2011) *A new prognostic bulk microphysics scheme for the IFS*. ECMWF Technical Memorandum 649, ECMWF, Reading.
- Forbes, R.M. and Ahlgrimm, M. (2014) On the representation of high-latitude boundary-layer mixed-phase cloud in the ECMWF global model. *Monthly Weather Review*, 142(9), 3425–3445.
- Forbes, R.M. and Tompkins, A.M. (2011) An improved representation of cloud and precipitation. *ECMWF Newsletter*, 129, 13–18.

- Harrington, J.Y., Meyers, M.P., Walko, R.L. and Cotton, W.R. (1995) Parameterization of ice crystal conversion processes due to vapor deposition for mesoscale models using double-moment basis functions. Part I: basic formulation and parcel model results. *Journal of the Atmospheric Sciences*, 52(23), 4344–4366.
- Hersbach, H., Bell, B., Berrisford, P., Hirahara, S., Horányi, A., Muñoz-Sabater, J., Nicolas, J., Peubey, C., Radu, R., Schepers, D., Simmons, A., Soci, C., Abdalla, S., Abellan, X., Balsamo, G., Bechtold, P., Biavati, G., Bidlot, J., Bonavita, M., De Chiara, G., Dahlgren, P., Dee, D., Diamantakis, M., Dragani, R., Flemming, J., Forbes, R., Fuentes, M., Geer, A., Haimberger, L., Healy, S., Hogan, R.J., Hólm, E., Janisková, M., Keeley, S., Laloyaux, P., Lopez, P., Lupu, C., Radnoti, G., de Rosnay, P., Rozum, I., Vamborg, F., Villaume, S. and Thépaut, J.-N. (2020) The ERA5 global reanalysis. *Quarterly Journal of the Royal Meteorological Society*, 146, 1999–2049.
- Hersbach, H., Bell, B., Berrisford, P., Horányi, A., Sabater, J.M., Nicolas, J., Radu, R., Schepers, D., Simmons, A., Soci, C. and Dee, D. (2019) Global reanalysis: goodbye ERA-Interim, hello ERA5. *ECMWF Newsletter*, 159, 17–24.
- Hobbs, P.V. (1974) *Ice Physics*, Vol. XVII. Oxford: Clarendon Press, p. 833.
- Hong, S.-Y., Dudhia, J. and Chen, S.-H. (2004) A revised approach to ice microphysical processes for the bulk parameterization of clouds and precipitation. *Monthly Weather Review*, 132, 103–120.
- Hong, S.-Y. and Pan, H.-L. (1996) Nonlocal boundary layer vertical diffusion in a medium-range forecast model. *Monthly Weather Review*, 124(10), 2322–2339.
- Hu, Z. and He, G.F. (1988) Numerical simulation of microphysical processes in cumulonimbus—Part I: microphysical model. *Journal of Meteorological Research*, 2(4), 471–489.
- Huang, L., Chen, D., Deng, L., Xu, Z., Yu, F., Jiang, Y. and Zhou, F. (2017) Main technical improvement of GRAPES_Meso V4.0 and verification. *Journal of Applied Meteorological Science*, 28(1), 25–37 (in Chinese).
- Iguchi, T., Matsui, T., Shi, J., Tao, W.K., Khain, A.P., Hou, A., Cifelli, R., Heymsfield, A. and Tokay, A. (2012) Numerical analysis using WRF-SBM for the cloud microphysical structures in the C3VP field campaign: impacts of supercooled droplets and resultant riming on snow microphysics. *Journal Geophysical Research*, 117, D23206.
- Intergovernmental Panel on Climate Change (IPCC) (2001) Climate Change 2001: The Scientific Basis, Contribution of Working Group I to the Third Assessment Report of the Intergovernmental Panel on Climate Change, J. T. Houghton et al., 881 pp., Cambridge Univ. Press, New York, NY.
- Jouan, C. and Milbrandt, J.A. (2019) The importance of the ice-phase microphysics parameterization for simulating the effects of changes to CCN concentrations in deep convection. *Journal of the Atmospheric Sciences*, 76, 1727–1752.
- Kang, Y., Jin, S., Peng, X., Yang, X., Shang, K. and Wang, S. (2018) Comparative analysis of single-moment and double-moment microphysics schemes in WRF on the torrential rainfall event in North China during 19–21 July 2016. *Plateau Meteorology*, 37(2), 481–494 (in Chinese).
- Koenig, L.R. (1972) Parameterization of ice growth for numerical calculations of cloud dynamics. *Monthly Weather Review*, 100(6), 417–423.
- Li, H., Li, J., Lin, W., Meng, W., Xiao, H. and Wang, A. (2011) Simulation study on microphysical process of freezing-rain event in southern China during the early 2008. *Plateau Meteorology*, 30(4), 942–950 (in Chinese).
- Linus, M. and Erland, K. (2013) Factors influencing skill improvements in the ECMWF forecasting system. *Monthly Weather Review*, 141, 3142–3153.
- Ma, Z., Liu, Q., Sun, J., Kong, Q., Li, Z., Shen, X., Zhao, C., Dai, K. and Tao, F. (2021a) The preliminary study on the reason to overestimation of a snowfall case by WSM6 scheme over North China. *Meteorological Monthly*, accepted (in Chinese).
- Ma, Z., Liu, Q., Zhao, C., Shen, X., Wang, Y., Jiang, J.H., Li, Z. and Yung, Y. (2018) Application and evaluation of an explicit prognostic cloud cover scheme in GRAPES global forecast system. *Journal of Advances in Modeling Earth Systems*, 10(3), 652–667.
- Ma, Z., Zhao, C., Gong, J., Zhang, J., Li, Z., Sun, J., Liu, Y., Chen, J. and Jiang, Q. (2021b) Spin-up characteristics with three types of initial fields and the restart effects on forecast accuracy in the GRAPES global forecast system. *Geoscientific Model Development*, 14, 205–221.
- Mason, B.J. (1971) *The Physics of Clouds*. New York, NY: Oxford University Press, p. 671.
- Mcmillen, J.D. and Steenburgh, W.J. (2015) Impact of microphysics parameterizations on simulations of the 27 October 2010 Great Salt Lake-effect snowstorm. *Weather and Forecasting*, 30, 136–152.
- Merion, A., García-Ortega, E., Fernández-González, S., Díaz-Fernández, J., Quitián-Hernández, L., Martín, M.L., López, L., Marcos, J.L., Valero, F. & Sánchez, J.L. (2019) Aircraft Icing: In-Cloud Measurements and Sensitivity to Physical Parameterizations. *Geophysical Research Letters*, 46, 11,559–11,567.
- Milbrandt, J.A., Yau, M.K., Mailhot, J., Bélair, S. and McTaggart-Cowan, R. (2010) Simulation of an orographic precipitation event during IMPROVE-2. Part II: sensitivity to the number of moments in the bulk microphysics scheme. *Monthly Weather Review*, 138, 625–642.
- Mlawer, E.J., Taubman, S.J., Brown, P.D., Iacono, M.J. and Clough, S.A. (1997) Radiative transfer for inhomogeneous atmospheres: RRTM, a validated correlated-k model for the longwave. *Journal Geophysical Research*, 102, 16,663–16,682.
- Molthan, A.L. and Colle, B.A. (2012) Comparisons of single- and double-moment microphysics schemes in the simulation of a synoptic-scale snowfall event. *Monthly Weather Review*, 140, 2982–3002.
- Molthan, A.L., Colle, B.A., Yuter, S.E. and Stark, D. (2016) Comparisons of modeled and observed reflectivities and fall speeds for snowfall of varied riming degrees during winter storms on Long Island, New York. *Monthly Weather Review*, 144, 4327–4347.
- Morrison, H. and Milbrandt, J.A. (2015) Parameterization of cloud microphysics based on the prediction of bulk ice particle properties. Part I: scheme description and idealized tests. *Journal of the Atmospheric Sciences*, 311, 287–311.
- Morrison, H., Milbrandt, J.A., Bryan, G.H., Ikeda, K., Tessendorf, S.A. and Thompson, G. (2015) Parameterization of cloud microphysics based on the prediction of bulk ice particle properties. Part II: case study comparisons with observations and other schemes. *Journal of the Atmospheric Sciences*, 72, 312–339.

- Morrison, H., Thompson, G. and Tatarki, V. (2009) Impact of cloud microphysics on the development of trailing stratiform precipitation in a simulated squall line: comparison of one- and two-moment schemes. *Monthly Weather Review*, 137, 991–1007.
- Nie, H., Liu, Q. and Ma, Z. (2016) Simulation and analysis of heavy precipitation using cloud microphysical scheme coupled with high-resolution GRAPES model. *Meteorological Monthly*, 42(12), 1431–1444 (in Chinese).
- Pincus, R., Batastone, C.P., Hofmann, R.J.P., Taylor, K.E. and Glecker, P.J. (2008) Evaluating the present-day simulation of clouds, precipitation, and radiation in climate models. *Journal Geophysical Research*, 113, D14209.
- Pruppacher, H.R. and Klett, J.D. (1978) *Microphysics of Clouds and Precipitation*. Dordrecht, Holland: D. Reidel Publishing Company, p. 714.
- Roebber, P.J., Bruening, S.L., Schultz, D.M. and Cortinas, J.R.J.V. (2003) Improving snowfall forecasting by diagnosing snow density. *Weather and Forecasting*, 18, 264–287.
- Rutledge, S.A. and Hobbs, P.V. (1983) The mesoscale and microscale structure and organization of clouds and precipitation in mid-latitude cyclones. Part VIII: a model for the “seeder-feeder” process in warm-frontal rainbands. *Journal of the Atmospheric Sciences*, 40, 1185–1206.
- Shen, X., Su, Y., Hu, J., Wang, J., Sun, J., Xu, J., Han, W., Zhang, H., Lu, H., Zhang, H., Chen, Q., Liu, Y., Liu, Q., Ma, Z., Jin, Z., Li, X., Liu, K., Zhao, B., Zhou, B., Gong, J., Chen, D. and Wang, J. (2007) Development and operational transformation of GRAPES global middle-range forecast system. *Journal of Applied Meteorological Science*, 28(1), 1–10 (in Chinese).
- Stoelinga, M.T. (2005) *Simulated Equivalent Reflectivity Factor As Currently Formulated in RIP: Description and Possible Improvements*. Seattle, WA: University of Washington Tech, p. 5.
- Su, Y., Shen, X., Peng, X., Li, X., Wu, X., Zhang, S. and Chen, X. (2013) Application of PRM scalar advection scheme in GRAPES global forecast system. *Chinese Journal of Atmospheric Sciences*, 37(6), 1309–1325 (in Chinese).
- Su, Y., Zhao, C., Wang, Y. and Ma, Z. (2020) Spatiotemporal variations of precipitation in China from surface gauge observations from 1961 to 2016. *Atmosphere*, 11(3), 303.
- Sun, J., Wang, P., Li, X. and Lu, Y. (2007) Numerical study on microphysical processes of two different snow cases in North China. *Acta Meteorologica Sinica*, 65(1), 29–44 (in Chinese).
- Taylor, K.E. (2001) Summarizing multiple aspects of model performance in a single diagram. *Journal Geophysical Research: Atmospheres*, 106(D7), 7183–7192.
- Thériault, J.M. and Stewart, R.E. (2010) A parameterization of the microphysical processes forming many types of winter precipitation. *Journal of the Atmospheric Sciences*, 67(5), 1492–1508.
- Thompson, G., Rasmussen, R.M. and Manning, K. (2004) Explicit forecasts of winter precipitation using an improved bulk microphysics scheme. Part I: description and sensitivity analysis. *Monthly Weather Review*, 132, 519–542.
- Walko, R.L., Cotton, W.R., Meyers, M.P. and Harrington, J.L. (1995) New RAMS cloud microphysics parameterization. Part I: the single moment scheme. *Atmospheric Research*, 38, 29–62.
- Wang, K., Zhang, F.M., Sun, C. and Wang, D. (2014) Development and validation of WRF-WSM3 scheme in simulation of snowstorm in the Tibetan plateau. *Chinese Journal of Atmospheric Sciences*, 38(1), 101–109 (in Chinese).
- Wu, W., Deng, L. and Wang, S. (2011) A numerical simulation of snowstorm in North China during 9–11 November 2009 and its cloud microphysics. *Meteorological Monthly*, 37(8), 991–998 (in Chinese).
- Wu, W., Liu, Y. and Betts, A.K. (2012) Observationally based evaluation of NWP reanalyses in modeling cloud properties over the southern Great Plains. *Journal Geophysical Research: Atmospheres*, 117, D12202.
- Yu, R., Zhang, Y., Wang, J., Li, J., Chen, H., Gong, J. and Chen, J. (2019) Recent progress in numerical atmospheric modeling in China. *Advances in the Atmospheric Sciences*, 36(8), 938–960.
- Yu, X., Yu, Z., Tang, Y. and Zhao, L. (2017) Influence of different cloud microphysical schemes on forecasts of a cold-front snowstorms in Xinjiang. *Torrential Rain and Disasters*, 36(1), 33–41 (in Chinese).
- Zhang, L., Liu, Y., Liu, Y., Gong, J., Lu, H., Jin, Z., Tian, W., Liu, G., Zhou, B. and Zhao, B. (2019) The operational global four-dimensional variational data assimilation system at the China Meteorological Administration. *Quarterly Journal of the Royal Meteorological Society*, 145, 1882–1896.
- Zhao, C., Jiang, Z., Sun, X., Li, W. and Li, L. (2020) How well do climate models simulate regional atmospheric circulation over East Asia? *International Journal of Climatology*, 40, 220–234.
- Zhao, C., Liu, L., Wang, Q., Qiu, Y., Wang, W., Wang, Y. and Fan, T. (2016) Toward understanding the properties of high ice clouds at Naqu site over the Tibetan plateau using ground-based active remote sensing measurements obtained during a short period in July 2014. *Journal of Applied Meteorology and Climatology*, 55(11), 2493–2507.
- Zhao, C., Liu, L., Wang, Q., Qiu, Y., Wang, Y. and Wu, X. (2017) MMCR-based characteristic properties of non-precipitating cloud liquid droplets at Naqu site over Tibetan plateau in July 2014. *Atmospheric Research*, 190, 68–76.
- Zhao, C., Xie, S., Klein, S.A., Protat, A., Shupe, M.D., McFarlane, S.A., Comstock, J.M., Delanoe, J., Deng, M., Dunn, M., Hogan, R.J., Huang, D., Jensen, M.P., Mace, G.G., McCoy, R., O’Connor, E.J., Turner, D.D. and Wang, Z. (2012) Toward understanding of differences in current cloud retrievals of ARM ground-based measurements. *Journal of Geophysical Research*, 117, D10206.
- Zhu, L., Gong, J., Huang, L., Chen, D., Jiang, Y. and Deng, L. (2017) Three-dimensional cloud initial field created and applied to GRAPES numerical weather prediction nowcasting. *Journal of Applied Meteorological Science*, 28(1), 38–51 (in Chinese).

How to cite this article: Ma, Z., Milbrandt, J.A., Liu, Q., Zhao, C., Li, Z., Tao, F. et al. (2021) Sensitivity of snowfall forecast over North China to ice crystal deposition/sublimation parameterizations in the WSM6 cloud microphysics scheme. *Quarterly Journal of the Royal Meteorological Society*, 147(739), 3349–3372.
Available from: <https://doi.org/10.1002/qj.4132>

APPENDIX A**T A B L E A1** Abbreviation and description of each microphysical process in the WSM6 scheme

No.	Abbreviation	Description
01	ccond	Condensation of cloud water
02	cevap	Evaporation of cloud water
03	rcond	Condensation of rain
04	revap	Evaporation of rain
05	pvi	Initiation nucleation of ice crystal
06	idep	Deposition of ice crystal
07	isub	Sublimation of ice crystal
08	sdep	Deposition of snow
09	ssub	Sublimation of snow
10	gdep	Deposition of graupel
11	gsub	Sublimation of graupel
12	fqci	Homogeneous freezing of cloud water below -40°C
13	pfrzc	Heterogeneous freezing of cloud water when $-40^{\circ}\text{C} < T < 0^{\circ}\text{C}$
14	mqci	Instantaneous melting of cloud ice when $T > 0^{\circ}\text{C}$
15	paacw	Accretion of cloud water by averaged snow/graupel
16	praut	Autoconversion rate from cloud to rain
17	pracw	Accretion of cloud water by rain
18	psacrs	Accretion of rain by snow to snow
19	piacrs	Accretion of rain by cloud ice to snow
20	pseml	Enhanced melting of snow by accretion of water
21	psmlt	Melting of snow to rain
22	pgeml	Enhanced melting of graupel by accretion of water to rain
23	pgmlt	Melting of graupel to rain
24	pfrzr	heterogeneous freezing of cloud water to ice crystal
25	pgacr	Accretion of rain by graupel
26	psacrg	Accretion of rain by snow to graupel
27	piacrg	Accretion of rain by cloud ice to graupel
28	pgaci	Accretion of cloud ice by graupel
29	pracig	Accretion of cloud ice by rain to graupel
30	psaut	Conversion (aggregation) of ice to snow
31	pracis	Accretion of cloud ice by rain to snow
32	psaci	Accretion of cloud ice by snow
33	pgaut	Conversion(aggregation) of snow to graupel
34	pracs	Accretion of snow by rain to graupel

APPENDIX B

TABLE B1 List of symbols for variables and parameters

Symbol	Description	Value
\dot{r}	Ice crystal deposition/sublimation rate	
M_I	Mean mass of ice crystal	
\bar{D}_I	Mean diameter of ice crystal	
S_I	Ice saturation	
N_I	Number concentration of ice crystal	
A_I	Thermodynamic function	
B_I	Thermodynamic function	
$\bar{D}_{I_{con}}$	Coefficient for mass–diameter relationship of ice crystals	11.9
ρ_a	Density of air	
q_I	Mixing ratio of ice crystal	
K_a	Thermal conductivity of air	
D_v	Diffusivity of water vapor in air	
L_s	Latent heat of sublimation	
R_v	Gas constant for water vapor	
P_{si}	Saturation vapor pressure over ice	
q_{si}	Saturation specific humidity over ice	
q_{sw}	Saturation specific humidity over water	
q_v	Specific humidity of environment	
T	Air temperature	
$n(D)$	Number concentration between D and $D + dD$	
D	Diameter of ice crystal	
dm/dt	Mass growth rate of ice crystal	
m	Mass of single ice crystal	
t	Model time	
C_i	Crystal capacitance term	
$G_i(T, P)$	Function defined in Pruppacher and Klett, 1978.	
f_{v,L^*}	Ventilation coefficient	
A	Aspect ratio of ice crystal	
c	Maximum dimension of ice crystal	
$\chi(A)$	Function of aspect ratio	
$\Gamma(n)$	Complete gamma function	
v	Shape parameter	1
λ	Slope parameter	
\bar{D}	Mean ice crystal size of number distribution	
D_n	Size related to \bar{D}	
$I(P)$	Moments of the gamma distribution	
Ψ	Function parameter	
a_1	Diffusion growth parameter in Koenig (1972)	
a_2	Diffusion growth parameter in Koenig (1972)	
QMR_{xy}	Conversion rate of a specific microphysical process	
$\Delta\sigma$	Height difference between two sigma levels	
WVL	Total integrated water vapor loss	
R	Pearson correlation coefficient	
$RMSE$	Centered root-mean-square difference	
σ	Standard deviation	
M_n	Simulated precipitation amount	
O_n	Observed precipitation amount	
CC_x	Column content of a specific hydrometeor	
q_x	Mass mixing ratio of a specific hydrometeor	
$ntop$	Total model levels	